iScience

Article

Astrocyte-induced firing in primary afferent axons

Graphical abstract

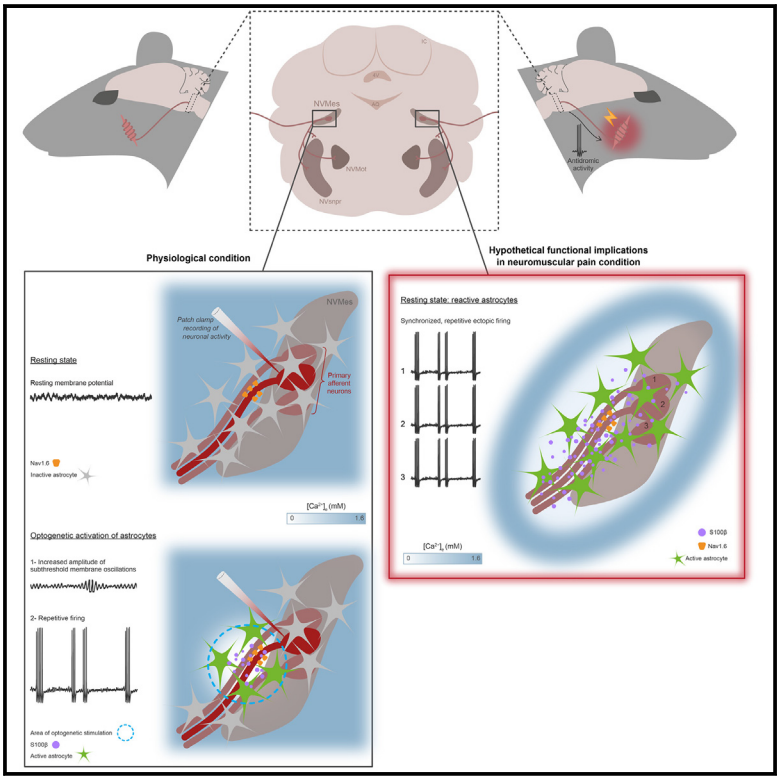

Highlights

- Stimulation of astrocytes along axons of primary afferents induces firing
- This firing is reminiscent of ectopic firing seen in afferents in pathological pain
- It involves a Nav1.6-channels mediated current that augments with $[Ca^{2+}]e$ decreases
- The astrocytes-induced firing relies on release of S100β, a Ca^{2+}-binding protein

Authors

Fanny Gaudel, Julia Giraud, Philippe Morquette, Marc Couillard-Larocque, Dorly Verdier, Arlette Kolta

Correspondence

arlette.kolta@umontreal.ca

In brief

Neuroscience; Cell biology

Gaudel et al., 2025, iScience *28*, 112006
March 21, 2025
https://doi.org/10.1016/j.isci.2025.112006

CellPress

iScience

CellPress
OPEN ACCESS

Article

Astrocyte-induced firing in primary afferent axons

Fanny Gaudel,[1,2,5] Julia Giraud,[1,5] Philippe Morquette,[1,4] Marc Couillard-Larocque,[1] Dorly Verdier,[1,2,6] and Arlette Kolta[1,2,3,6,7,*]

[1]Département de Neurosciences, Université de Montréal, Montréal, QC, Canada
[2]Centre Interdisciplinaire de Recherche sur le Cerveau et l'Apprentissage, Université de Montréal, Montréal, QC, Canada
[3]Faculté de Médecine Dentaire, Université de Montréal, Montréal, QC, Canada
[4]F. M. Kirby Neurobiology Center and Department of Neurology, Boston Children's Hospital and Harvard Medical School, Boston, MA 02115, USA
[5]These authors contributed equally
[6]Senior author
[7]Lead contact
*Correspondence: arlette.kolta@umontreal.ca
https://doi.org/10.1016/j.isci.2025.112006

SUMMARY

The large-caliber primary afferents innervating the spindles of the jaw-closing muscles have their cell bodies located centrally in the mesencephalic trigeminal nucleus (NVmes). We have shown, in an acid-induced jaw muscle chronic myalgia model, that these afferents exhibit increased excitability and ectopic discharges that emerge from subthreshold membrane oscillations (SMOs) supported by a persistent sodium current (I_{NaP}) exquisitely sensitive to extracellular Ca^{2+}-decreases. Here, we explore if the Ca^{2+}-binding astrocytic protein, S100β, contributes to this hyperexcitability emergence and aim to localize the site where ectopic discharge arises using whole-cell patch-clamp recordings on mice brain slices. We found that astrocytes, by lowering $[Ca^{2+}]_e$ at focal points along the axons of NVmes neurons through S100β, enhance the amplitude of the $Na_V1.6$-dependent SMOs, leading to ectopic firing. These findings suggest a crucial role for astrocytes in excitability regulation and raise questions about this neuron-astrocyte interaction as a key contributor to hyperexcitability in several pathologies.

INTRODUCTION

The primary afferents (PAs) innervating the spindles of the jaw-closing muscles and the pressoreceptors of the periodontal ligaments have their somata in the mesencephalic trigeminal nucleus (NVmes), located centrally in the brainstem, where they receive inputs from several structures in the forebrain, mid-brain,[1–3] and lower brainstem.[4–7] These neurons exhibit voltage-dependent rapid subthreshold membrane oscillations (SMOs) that greatly influence cellular excitability since they often lead to repetitive firing. Both the SMOs and repetitive firing properties of NVmes neurons rely on a persistent sodium current (I_{NaP})[8–12] and evidence of a strong contribution of $Na_V1.6$ channels to I_{NaP} and SMOs has been shown in these neurons.[8] However, it is known that the $Na_V1.6$ channels distribution is not uniform on the membrane of myelinated neurons: a higher concentration is found at the axon initial segment (AIS) and the nodes of Ranvier[13–18] where they contribute to the action potential initiation and propagation, respectively. This implies that in NVmes neurons, both activities may arise from their axon membrane electrical properties rather than the soma. Therefore, local modulation of axonal $Na_V1.6$ could have profound effect on these neurons output.

Variation of extracellular calcium concentration ($[Ca^{2+}]_e$) modulates voltage-gated sodium channels[19] and I_{NaP} in particular is enhanced by the decrease of $[Ca^{2+}]_e$. Our team has shown that astrocytes can play a key role in this mechanism through release of the Ca^{2+}-binding protein S100β, which by decreasing $[Ca^{2+}]_e$ and enhancing I_{NaP}, changes the discharge pattern of neurons in the trigeminal main sensory nucleus (NVsnpr)[20] and integration properties of layer 5 pyramidal neurons in the visual cortex.[21] We postulate that this neuron-astrocyte interaction occurs at a precise neuronal compartment in the NVmes where $Na_V1.6$ channels are enriched. We hypothesize that it could explain the reported excitability changes of the large-diameter PAs in various pain models, such as the acid-induced jaw muscle chronic myalgia model,[22] in which increased amplitude of the SMOs and spontaneous ectopic firing were observed, despite a hyperpolarizing shift in their firing and SMOs threshold. Thus, using a combination of whole-cell patch clamp recordings, local applications of Ca^{2+}-chelating agents, immunohistochemistry, and optogenetic activation of peri-axonal astrocytes, we tested whether manipulation of astrocytes or local decreases of $[Ca^{2+}]_e$ along the axons of NVmes neurons affect the SMOs and repetitive firing capability of these neurons through an S100β/$Na_V1.6$-dependent

Table 1. Electrophysiological characteristics of NVmes neurons

Electrophysiological characteristics	WT mice $N = 61$	GFAP-ChR2-EYFP mice $N = 99$	WT + GFAP-ChR2-EYFP mice $N = 160$	$Na_V1.6$ KO mice $N = 15$
RMP (mV)	−55 ± 0.5[a]	−54 ± 0.3[a]	−54 ± 0.2	−56 ± 0.9
Firing threshold (mV)	−42 ± 0.7[a]	−43 ± 0.4[a]	−43 ± 0.4[b]	−37 ± 1.8[b]
Input resistance (MΩ)	83 ± 8[a]	82 ± 5[a]	82 ± 4	70 ± 8

Values are mean ± SEM.
ChR2, channelrhodopsin 2; EYFP, enhanced yellow fluorescent protein; GFAP, glial fibrillary acidic protein; KO, knock-out; NVmes, mesencephalic trigeminal nucleus; N, number of neurons; RMP, resting membrane potential; WT, wild type.
[a]$p > 0.05$ for comparisons of the 3 parameters between WT and GFAP-ChR2-EYFP mice, Kruskall-Wallis test.
[b]$p = 0.03$, Kruskall-Wallis test with Bonferroni correction.

mechanism. We found that locally chelating the calcium around the axons of NVmes neurons increases the SMOs amplitude and hyperpolarizes the SMOs and firing thresholds thereby increasing the occurrence of repetitive firings in these neurons. We also found that astrocytes are closely positioned next to the $Na_V1.6$ immunopositive axons of the NVmes neurons and that their optogenetic activation enhances $Na_V1.6$-dependent SMOs leading to ectopic firing through the release of S100β along the axons of NVmes neurons.

RESULTS

Electrophysiological properties of NVmes neurons

One hundred and sixty neurons recorded in the mesencephalic trigeminal nucleus (NVmes) of 44 wild-type (WT) mice and 68 mice expressing the channel-rhodopsin 2 (ChR2) under the control of the glial fibrillary acidic protein (GFAP) promoter (GFAP-ChR2 mice) fulfilled the inclusion criteria. The recorded neurons were filled with Alexa Fluor (488 or 594), and all showed the typical pseudo-unipolar morphology of primary sensory afferents consisting of a spherical or ovoid cell body attached to a single process. Their basic electrophysiological characteristics are summarized in Table 1. There were no statistical differences in the resting membrane potential (RMP), the input resistance, and the firing threshold between neurons recorded from WT and GFAP-ChR2 mice (Table 1, Kruskall-Wallis test, $p > 0.05$). Therefore, all the data obtained from both mice lines were pooled together. The pooled neurons had a RMP of −54 ± 0.2 mV, a firing threshold of −43 ± 0.4 mV, and an input resistance of 82 ± 4 MΩ. All the recorded neurons showed a strong inward rectification producing a prominent sag (Figure 1A, arrow) upon membrane hyperpolarization, typical of these cells, while 96 (60%) of them fired a rebound action potential at the offset of the hyperpolarizing pulses (Figure 1A, arrowhead). Accommodation of firing upon membrane depolarization occurred in 120 of the 160 (75%) neurons, with 68 (57%) of them discharging only a single action potential (Figure 1A), even with long-duration (up to 1,000 ms) pulses. The I-V curve shown in Figure 1A is typical of the accommodating NVmes neurons and reveals an outward rectification during depolarization and an inward rectification during hyperpolarization, both emphasized by the linear fitting (red straight line) of the non-rectifying portion of the I-V curve. The 40 (25%) cells that did not show firing accommodation either fired recurrent bursts ($n = 30$) as illustrated in Figure 1B or fired without pause for the duration of the depolarizing pulses ($n = 10$; Figure 1C). Thus, the recorded NVmes neurons in mice could be classified into the same three subtypes reported by Yang et al.[23] in rats: the spike-adaptative, the burst-firing, and the tonic-firing neurons. All the burst-firing neurons exhibited voltage-dependent subthreshold membrane potential oscillations (SMOs, inset in Figure 1B, right) while only 32 (27%) out of the 120 adaptative neurons exhibited such activity. SMOs, most of the time, could not be sampled in the tonic-firing neurons since they tend to fire repetitively when depolarized. The mean frequency of this oscillatory activity in 30 burst-firing and 32 spike-adaptative NVmes neurons was 82 ± 3 Hz, their averaged peak-to-peak amplitude was 1.5 ± 0.1 mV and they appeared at an average threshold membrane potential of −45 ± 0.6 mV as determined by a ramp current injection protocol. As already shown in numerous studies in rats[10,24] and mice,[25] these SMOs were suppressed by membrane hyperpolarization (Figure 1D, bottom trace), and increased in amplitude with membrane depolarization until strong repetitive firing was elicited (Figure 1D, top trace). When measured in bursting neurons in which clear SMOs could be seen next to a burst ($n = 25$), the SMOs frequency in each cell (*black* dots in graph in Figure 1D) paralleled the intra-burst firing frequency (*gray* dots in graph in Figure 1D) and were significantly correlated (linear regression, $r = 0.96$, $p < 0.001$), indicating that these SMOs are a key factor that contributes to greater cellular excitability. The SMOs are supported by I_{NaP},[10,24,25] and we as others[23] have hypothesized that any factor that impacts I_{NaP} will indirectly modulate the excitability of these neurons.

Axonal applications of Ca^{2+}-chelators cause firing in NVmes neurons

Our previous work, using whole-cell recordings of NVsnpr and cortical neurons, has demonstrated the ability to modulate I_{NaP} or I_{NaP}-dependant neuronal activity by producing local decreases of Ca^{2+} with local applications of Ca^{2+}-chelators such as 1,2-bis(*o*-aminophenoxy)ethane-*N*,*N*,*N*′,*N*′-tetraacetic acid (BAPTA) or S100β,[20,21] a protein synthesized and released by astrocytes,[26] that binds Ca^{2+}. Using a similar approach here to test the effect of I_{NaP} modulation on the excitability of NVmes neurons, BAPTA or S100β were locally applied near the soma or the stem axon of 40 neurons from 29 mice and 31 neurons from 21 mice, respectively. To alleviate the text, all the numbers related to the effects of these applications are reported in Table 2. The only observed effect of either BAPTA or S100β applications near the soma was a long-lasting hyperpolarization that

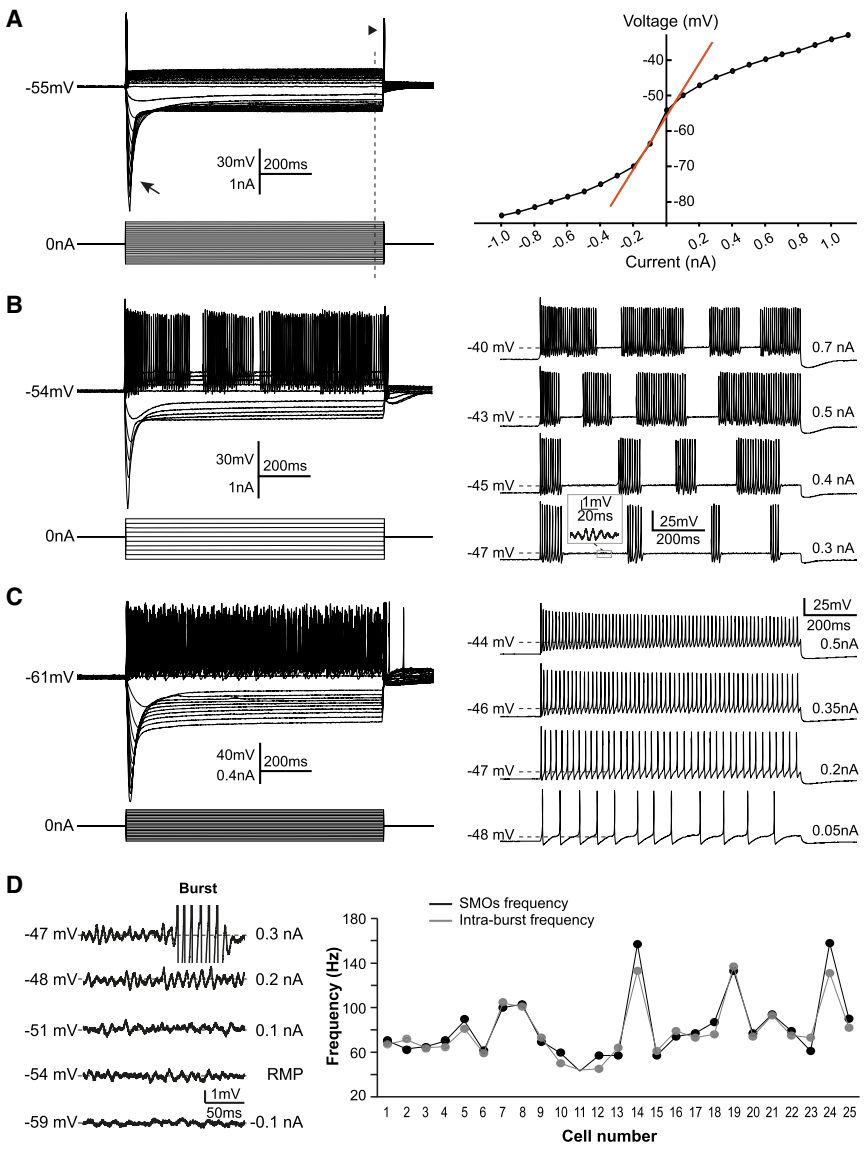

Figure 1. Diversity of NVmes neurons firing profiles

(A–C) Left, top traces: membrane responses of a spike-adaptative (A), a burst-firing (B), and a tonic-firing (C) NVmes neuron to injections of hyperpolarizing and depolarizing current pulses (*bottom* traces). The arrow and arrowhead point the sag and the rebound action potential, respectively. The vertical dotted line indicates the position of the membrane voltage and the current injection lecture for the I-V curve. (A) *Right*: I-V curve showing the inward and outward membrane rectification of a spike-adaptative neuron in response to hyperpolarizing and depolarizing injected current, respectively. The red line is the linear fitting to the non-rectifying portion of the I-V curve. (B and C) *Right*: isolated traces to distinguish bursting and tonic firing profiles. Inset in (B, *right*) shows SMOs in a burst-firing NVmes neuron. (D) *Left*: membrane voltage recordings showing the effect of membrane potential on the SMOs. They are abolished with membrane hyperpolarization (*bottom* trace), and lead to firing with membrane depolarization (*top* trace). (D) *Right*: plot of the intra-burst firing frequency (*gray* dots) and SMOs frequency (*black* dots) in 25 NVmes neurons at the bursting threshold for each cell showing how they parallel each other.

I-V, current-voltage; NVmes, mesencephalic trigeminal nucleus; RMP, resting membrane potential; SMOs, subthreshold membrane oscillations.

outlasted the duration of the applications by about 13 and 7s respectively (Table 2; Figure 2A). Axonal applications of either BAPTA or S100β elicited similar hyperpolarizations only in 13% of cases (Figure 2B, top two traces), a depolarization in a single case with each and no effects in a few cases (Table 2). The most prevalent effect was induction of firing (Table 2; Figure 2B, third to fifth traces) that often overrode a depolarizing plateau (of 1.9 ± 0.1 mV in 36 BAPTA applications, and 1.3 ± 0.1 mV in 17 S100β applications; Figure 2B, third traces) or that was preceded or concomitant with a membrane potential hyperpolarization (of 1.1 ± 0.7 mV in 7 BAPTA applications and 2.8 ± 0.6 mV in 10 S100β applications, Figure 2B, fourth traces). In the remaining 10 and 6 applications of BAPTA or S100β, respectively, firing emerged directly from the resting potential without prior membrane potential change (Figure 2B, bottom traces). The vertical bar charts in Figure 2C illustrate the percentage of the different responses and the different firing patterns, respectively, observed in response to BAPTA (*blue* bars) or S100β (*purple* bars) application near the soma or axonal process of the recorded neurons.

Four different firing patterns were elicited by these axonal applications: high-frequency trains (60 ± 7 Hz, n = 16, and 52 ± 10 Hz, n = 5 for BAPTA and S100β, respectively; Figure 2D, top trace); recurrent bursting (inter-burst frequency: 5.5 ± 0.6 Hz, intra-burst frequency: 72 ± 6 Hz, n = 11, and interburst frequency: 7.2 ± 1.4 Hz and an intra-burst frequency: 68 ± 6 Hz, n = 9 for BAPTA and S100β, respectively; Figure 2B, fourth right trace; Figure 2D, second trace); low-frequency trains (12 ± 4 Hz, n = 7 and 3.8 ± 1.4 Hz, n = 8 for BAPTA and S100β, respectively; Figure 2D, third trace), and a mix of bursting and high- or low-frequency trains (n = 12 and 7, respectively, and n = 6 and 3 for BAPTA and S100β, respectively; Figure 2D, fourth and fifth traces, respectively). BAPTA applications induced more high-frequency trains while S100β triggered more bursting responses, although firing responses were distributed in all firing categories for both Ca^{2+} chelators and only S100β produced singlet firing (Figure 2E). As summarized in Figure 2F, bursting and high-frequency trains were observed in a majority of spike-adaptative neurons, but responses were distributed among the 3 types of recorded NVmes neurons.

Table 2. Effects of BAPTA and S100β applications on NVmes neurons

	Hyperpolarization			Firing				
	Latency (s)	Amplitude (mV)	Duration (s)	Latency (s)	Threshold (mV)	Duration (s)	Depolarization	No effect
Somatic BAPTA *n* = 23 *N* = 23	0.4 ± 0.1 (*n* = 23) *N* = 23	3.9 ± 0.4	24 ± 3 application 11 ± 1	–	–	–	–	–
Somatic S100β *n* = 25 *N* = 25	0.4 ± 0.1 (*n* = 25) *N* = 25	2.8 ± 0.3	18 ± 2 application 11 ± 1	–	–	–	–	–
Axonal BAPTA *n* = 69 *N* = 34	0.3 ± 0.03 (*n* = 9) *N* = 5	5 ± 0.9	22 ± 4 application 9 ± 1	1.2 ± 0.2 (*n* = 53) *N* = 31	−53 ± 1	4.5 ± 1.2 application 2.9 ± 0.3	(*n* = 1) *N* = 1	(*n* = 6) *N* = 3
Axonal S100β *n* = 46 *N* = 19	1 ± 0.4 (*n* = 6) *N* = 4	2.3 ± 0.5	32 ± 5 application 21 ± 4	2.6 ± 0.6 (*n* = 33) *N* = 19	−52 ± 0.9	2.7 ± 0.4 application 5 ± 1	(*n* = 1) *N* = 1	(*n* = 6) *N* = 4

Values are mean ± SEM.
Some neurons were tested at the soma and multiples sites along the axons.
n, number of applications; *N*, number of neurons; (*n*), number of responses; NVmes, mesencephalic trigeminal nucleus.

Axonal applications of BAPTA or S100β increase NVmes neurons' excitability by increasing SMOs and decreasing oscillation and firing threshold

Studies in biophysics have shown that extracellular Ca^{2+} ions exert a voltage-dependent partial block of Na^+ channels and that removal of this block not only increases the amplitude of the current in single-channel measurements,[19] but also shifts the activation gating range toward more hyperpolarized potentials.[27] Thus, we first examined whether BAPTA and S100β altered the voltage-dependent firing and SMOs characteristics of NVmes neurons since both depend on Na^+ channels. Given their similarity, BAPTA- and S100β-elicited firing responses were pooled together in this section for a total of 86 responses from 50 neurons. Those responses were elicited at an average RMP of −56 ± 1 mV and their threshold for firing was −52 ± 1 mV (Table 3). SMOs could be seen in 35 of the 86 firing responses from 28 neurons, 18 of which exhibited no SMOs before. In those responses, the SMOs were measured at an average RMP of −54 ± 1 mV, had an amplitude of 2.3 mV ± 0.1 mV, and a frequency of 71 ± 3 Hz (Table 3). A single response per neuron was considered for comparisons between controls and BAPTA or S100β induced effects (n = 50). BAPTA and S100β triggered firing at more hyperpolarized potentials than did standard step current injections (Figures 3A and 3B; Table 3, empty and solid black bars, Wilcoxon Signed-rank test, $p < 0.001$, $n = 50$). The shift of firing threshold toward hyperpolarized potentials was also seen when using a ramp current injection protocol (Figure 3C, red arrows; Table 3; Figure 3B, empty and solid gray bars, Student paired t test, $p < 0.001$, $n = 7$).

Similar observations were made when comparing SMOs that appear intermingled with the firing during step current injection ($n = 10$) or ramp current injection protocols ($n = 5$) to those elicited during BAPTA and S100β-induced firings. The latter appeared, during ramp current injection, at potentials 10–16 mV more hyperpolarized than the former (Figure 3C, black arrows; Table 3; Figure 3E, left vertical bars chart, Student paired t test, $p < 0.001$, $n = 5$). They also had a larger amplitude (Figures 3D and 3E; Table 3, middle vertical bars chart, Wilcoxon Signed-rank test, $p = 0.02$, $n = 10$) and a lower frequency (Table 3; Figure 3E, right vertical bars chart, Student paired t test, $p < 0.001$, $n = 10$) than the SMOs induced by depolarizing steps current injection. When measured in the bursting responses (n = 15/20 bursting responses) of 15 neurons, the SMOs frequency (*black* dots in the graph in Figure 3F) in each cell paralleled the intra-burst firing frequency (*gray* dots in the graph in Figure 3F) and both were significantly correlated (Figure 3G, linear regression, $r = 0.97$, $p < 0.001$).

I_{NaP} is responsible for BAPTA- or S100β-induced firing

SMOs and bursting in NVmes neurons rely on I_{NaP},[12] which in these neurons is associated partly with the $Na_V1.6$ isoform since it is significantly reduced, but not completely abolished in $Na_V1.6$ null mice.[25] To ascertain the involvement of I_{NaP} and $Na_V1.6$ containing channels in the firing-inducing action of BAPTA and S100β, we tested the effects of riluzole (a blocker of I_{NaP}) and 4,9-anhydro-tetrodotoxin (4,9-anhydro-TTX) (a blocker of sodium channels containing the $Na_V1.6$ α subunit[28]). The BAPTA-induced firing was abolished by bath-application of either riluzole (20 μM; not shown, n = 2/2) or 4,9-anhydro-TTX (0.1 μM; Figure 4A, $n = 7/7$). In two additional cells, the S100β-induced firing was also abolished by bath applications of 4,9-anhydro-TTX. However, the SMOs accompanying 7 of these firing responses were blocked in 3 cases and only slightly reduced in amplitude in the 4 remaining cases (2.2 ± 0.6 mV vs. 1.5 ± 0.6 mV; $p = 0.109$, Wilcoxon Signed-rank test). The input resistance and firing threshold of the recorded neurons were unchanged by 4,9-anhydro-TTX. However, the RMP was slightly but significantly

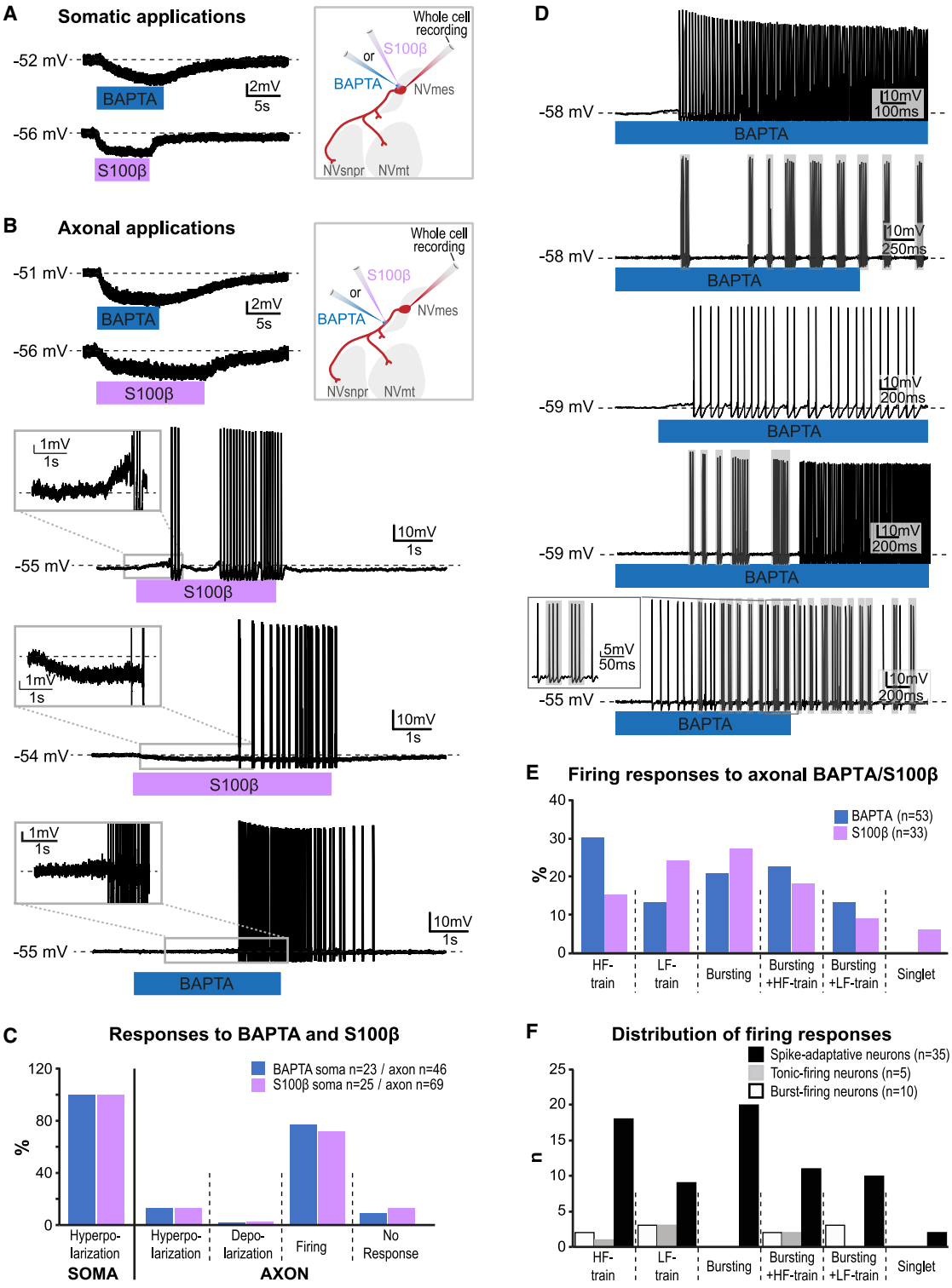

Figure 2. Chelation of extracellular calcium exerts a variety of effects on NVmes neurons

(A) Somatic applications of Ca^{2+} chelators BAPTA (*top* trace) and S100β (*bottom* trace) induce a slight and reversible hyperpolarization of NVmes neurons' membrane potential.

(legend continued on next page)

Table 3. Effects of BAPTA and S100β axonal applications on firing threshold and subthreshold membranes oscillations characteristics

	FIRINGS		SMOs			
	Vm (mV)	Threshold (mV)	Vm (mV)	Threshold (mV)	Amplitude (mV)	Frequency (Hz)
BAPTA and S100β applications (n = 86)/N = 50	−56 ± 1 (n = 86) N = 50	−52 ± 1	−54 ± 1 (n = 35/86) N = 28/50	_	2.3 ± 0.1	71 ± 3
Step current injections N = 50	_	−43 ± 1[a] N = 50	−43 ± 1[b] N = 10/50	_	1.5 ± 0.2[c]	92 ± 6[d]
BAPTA and S100β applications (n = 50)/N = 50	_	−52 ± 1[a] N = 50	−52 ± 1[b] N = 10/50	_	2.3 ± 0.2[c]	64 ± 4[d]
Ramp current injection N = 7	_	−37 ± 2 N = 7	_	−43 ± 2 N = 5	_	_
Ramp current injection + S100β application N = 7	_	−54 ± 2 N = 7	_	−60 ± 2 N = 5	_	_

Values are mean ± SEM.
N, number of neurons; (n), number of responses; SMOs, subthreshold membrane oscillations.
[a] $p < 0.001$, Wilcoxon Signed-rank test.
[b] $p < 0.01$, Student paired t test.
[c] $p < 0.05$, Wilcoxon Signed-rank test.
[d] $p < 0.001$, Student paired t test.

more hyperpolarized upon 4,9-anhydro-TTX application (−56 ± 3 mV vs. −58 ± 4 mV, $p = 0.016$, Student paired t test), suggesting that I_{NaP} may contribute to the RMP in these cells.

To ensure that the firing induced in NVmes neurons by axonal application of BAPTA or S100β did not involve some indirect activation of synaptic transmission, which may have been masked by the potent effect of the I_{NaP} blockers, we tested the effect of a cocktail of antagonists for the AMPA/kainate (CNQX, 10 μm), NMDA (AP5, 26 μm), and $GABA_A$ (gabazine, 20 μm) receptors. Bath application of the synaptic blockers cocktail did not abolish the firing triggered by local application of BAPTA (Figure 4B, middle trace) or S100β along the axonal process of 7 tested neurons (BAPTA, n = 4, S100β, n = 3).

To further ascertain the requirement of $Na_V1.6$ channels involvement in BAPTA or S100β-induced firing, both drugs were applied in the vicinity of NVmes neurons in $Na_V1.6$ knockout mice. These mice express a mutation identified as a small long interspersed nuclear element insertion into exon 2 of the Scn8a gene, which as a result encodes for a very short inactive protein.[29] The 15 neurons recorded from 5 $Na_V1.6$ knockout mice differed from those of WT/GFAP-ChR2 mice only for their firing threshold (−37 ± 2 mV; Kruskall Wallis test with Bonferroni correction, p = 0.03; Table 1). All showed an outward rectification during depolarization and an inward rectification during hyperpolarization (Figure 5A, right and left, red straight line: linear fitting to the non-rectifying portion of the I-V curve) producing a prominent sag upon membrane hyperpolarization (Figure 5A, arrow). All but one (14/15) showed, as the spike-adaptative subtype neurons, accommodation of firing upon membrane depolarization, with 12 of them discharging only a single action potential, even with long-duration pulses (up to 1,000 ms). Local applications of BAPTA were tested in 10 NVmes neurons with 5 somatic applications in 5 cells and 11 axonal applications in 7 cells. Only two of the somatic applications produced an effect that was a membrane hyperpolarization (of 0.7 and 1.2 mV at a latency of 0.4 and 0.6 s; Figure 5B, top trace), while axonal applications caused membrane hyperpolarization (−1.3 mV) once, depolarization in 3 cases (1.1 ± 0.2 mV), firing once (in one of the spike-adaptative neurons), and no response in the 6 remaining cases (Figure 5B, bottom trace).

Local applications of S100β were tested on 4 NVmes neurons from 2 $Na_V1.6$ knockout mice, with 2 somatic and 11

(B) Applications of Ca^{2+} chelators BAPTA or S100β along the axonal process of NVmes neurons induce cell hyperpolarization (*top* two traces) or firing, which could be preceded by membrane depolarization (*second* trace), hyperpolarization (*third* trace), or no change in membrane potential (*bottom* trace). *Middle insets:* cartoons illustrating the experimental set-ups. *Left insets:* zooms on the initial part of the firing responses.
(C) All somatic applications resulted in cell hyperpolarization, while most axonal applications triggered cell firing.
(D) This firing was observed in different patterns. Trains of high-frequency repetitive firing (*top* trace) were prominent in a majority of NVmes neurons. In some neurons, BAPTA triggered recurrent bursts (*second* trace), a train of low-frequency single action potentials (*third* trace), or a mix of neuronal bursting and train of high- or low-frequency action potentials (*fourth and fifth* traces, respectively) for the duration of BAPTA application.
(E) Bar chart quantifying the response profiles of NVmes neurons to somatic or axonal applications of BAPTA (*blue*), or S100β (*purple*) in WT/GFAP-ChR2 mice.
(F) Bar chart of the relative distribution of the neuronal firing responses elicited after axonal applications of BAPTA and S100β in the spike-adaptative (*black* bars), tonic-firing (*gray* bars), and burst-firing (*empty* bars) NVmes neurons.
ChR2, channelrhodopsin 2; GFAP, glial fibrillary acidic protein; HF, high-frequency; LF, low-frequency; NVmes, mesencephalic trigeminal nucleus; NVmt, trigeminal motor nucleus; NVsnpr, trigeminal main sensory nucleus.

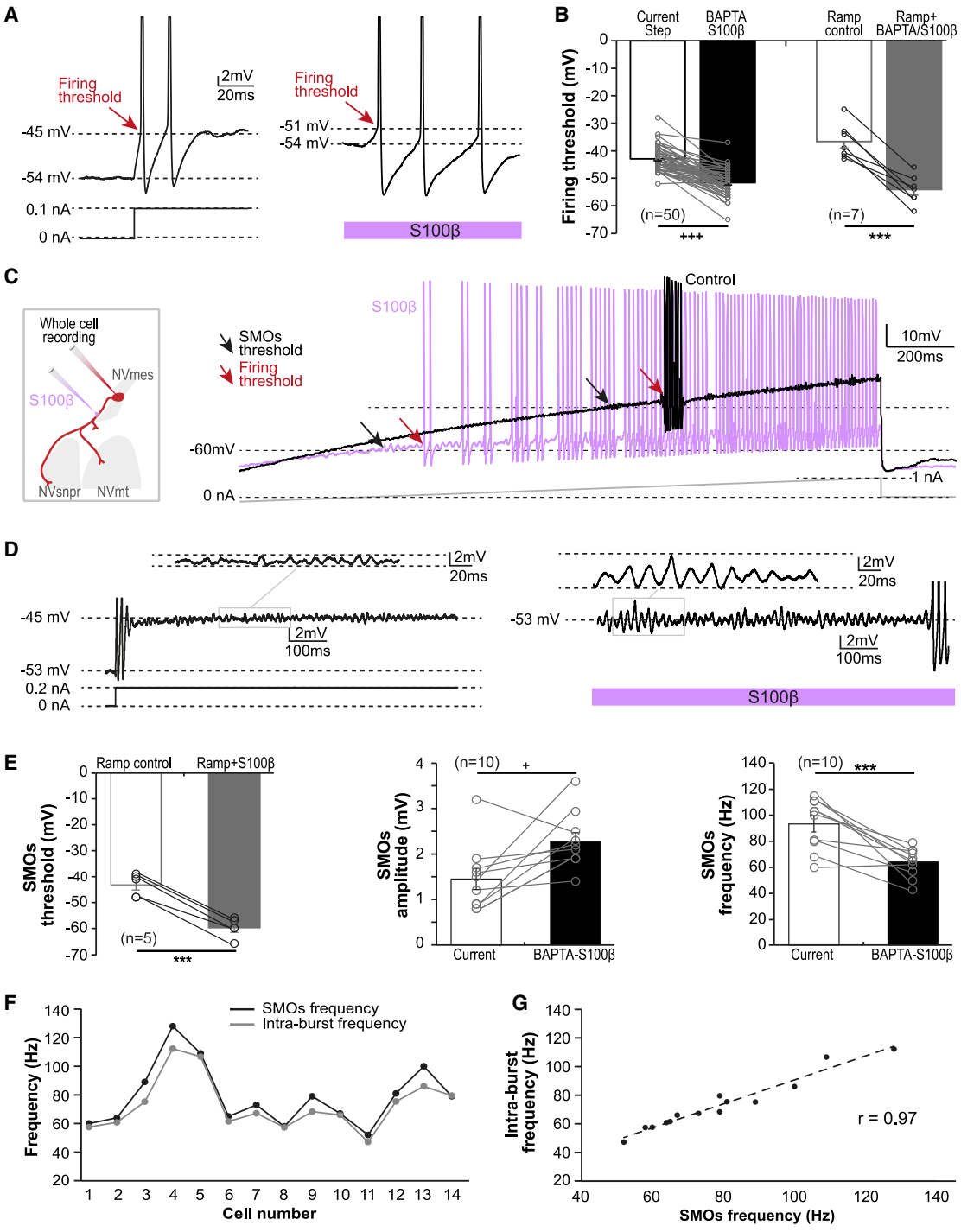

Figure 3. Lowering of SMOs and firing voltage thresholds of NVmes neurons by chelation of extracellular Ca^{2+} around their axonal processes

(A) Membrane voltage recordings of a NVmes neuron firing induced with depolarizing step current injection (*left* trace) or axonal application of S100β (*right* trace, setup illustrated in C) showing that S100β lowers the firing threshold.

(B) Bar chart comparing firing voltage threshold of 50 NVmes neurons with step current injections (*empty black* bar, as illustrated in A, *left* trace) and with BAPTA and S100β axonal applications (*solid black* bar, as illustrated in A, *right* trace). The gray bars show the firing voltage threshold of 7 NVmes neurons with ramp current injection (as illustrated in C) in control condition (*empty gray* bar) and during BAPTA and S100β applications near the axonal process (*solid gray* bar) of the recorded neurons.

(legend continued on next page)

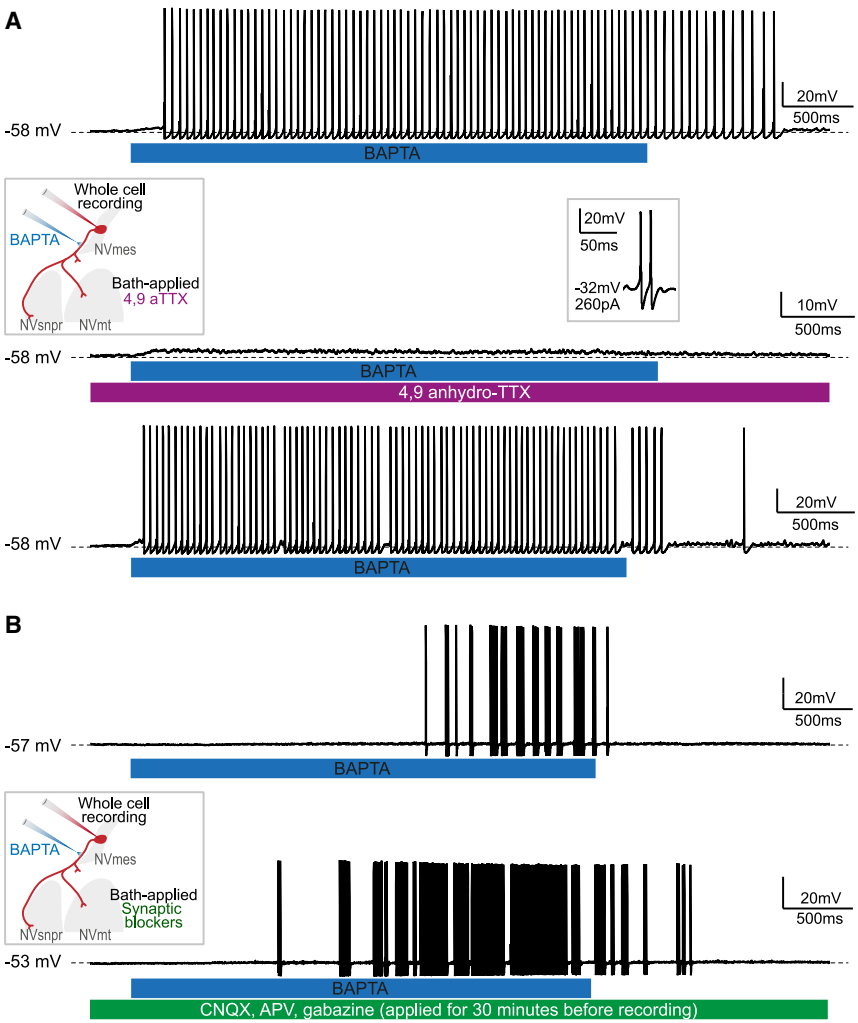

Figure 4. Axonal BAPTA- and S100β-induced firing in NVmes neuron persists in presence of synaptic blockers and appears to depend solely on I_{NaP} and the activity of $Na_V1.6$ channels

(A) Sustained firing recorded in a NVmes neuron following local application of BAPTA on its axonal process (*top*) is abolished in presence of 4,9-anhydro-TTX, a highly specific $Na_V1.6$ blocker (*middle*) and recovered after 40 min of washout of the 4,9-anhydro-TTX (*bottom*). The experimental setup is illustrated in the *left inset*, while the *right inset* shows that the neuron is still capable of firing with membrane depolarization by current injection in presence of 4,9-anhydro-TTX.

(B) Repetitive bursting recorded in a NVmes neuron following local application of BAPTA on its axonal process (*top*) persists after 30 min of bath application of glutamatergic and GABAergic blockers (respectively CNQX, APV and gabazine; *bottom*).

NVmes, mesencephalic trigeminal nucleus; NVmt, trigeminal motor nucleus; NVsnpr, trigeminal main sensory nucleus.

axonal applications. On the 2 somatic applications, only one produced a hyperpolarization (2.5 mV at a latency of 0.1 s), while the other had no effect. Seven of the axonal applications had no effect as well, while 4 caused a small hyperpolarization of 1.4 ± 0.1 mV at a latency of 0.5 ± 0.3 s. Figure 5C illustrates the relative distribution of the responses elicited by somatic and axonal applications of BAPTA or S100β (blue and purple bars, respectively) on NVmes neurons from $Na_V1.6$ knockout mice.

A precise axonal subregion is involved in the $Na_V1.6$-dependent firing

Knowing that the BAPTA and S100β-induced firing is I_{NaP}-dependent and that the $Na_V1.6$ channels that support I_{NaP} are enriched in the AIS and the nodes of Ranvier, we tried to narrow down the precise locations at which local decrease of $[Ca^{2+}]_e$ were more potent to elicit firing. Given the simple morphology of these neurons,

(C) Illustration of the experimental set-up (*left*), and recording (*right*) of a NVmes neuron while applying a ramp current injection (−1 to 1nA, the hyperpolarizing part is truncated) in control condition or during an axonal application of S100β (*black* and *purple* traces, respectively). S100β triggered neuronal repetitive firing by lowering the SMOs (*black arrows*, control: −39 mV vs. S100β: −59 mV) and firing (*red arrows*, control: −34 mV vs. S100β: −57 mV) voltage thresholds.

(D) Membrane voltage recordings of a NVmes neuron SMOs induced with depolarizing step current injection (*left* trace) or axonal application of S100β (*right* trace, as illustrated in B) showing that S100β increases SMOs amplitude in this neuron.

(E) *Left*: bar chart of SMOs voltage threshold of 5 NVmes neurons with ramp current injection in control condition (*empty gray* bar) and during S100β applications near their axonal process (*solid gray* bar). *Middle*: bar chart of the amplitude of the SMOs induced with depolarizing step current injection (*empty black* bar, as shown in D, *left*) or axonal application of BAPTA or S100β (*solid black* bar, as shown in D, *right*) in 10 NVmes neurons. *Right*: bar chart of the frequency of the SMOs induced with depolarizing step current injection (*empty black* bar, as shown in D, *left*) or axonal application of BAPTA or S100β (*solid black* bar, as shown in D, *right*) in 10 NVmes neurons.

(F) Plot of intra-burst firing frequency (*gray* dots) and SMOs frequency (*black* dots) in 14 neurons showing a parallel increase with both S100β and BAPTA.

(G) Scatterplot of intra-burst firing frequency and SMOs frequency in the BAPTA- or S100β-induced burst-firing responses showing a positive relationship between both variables. A linear regression (dotted line) between both variables shows that they are significantly correlated ($r = 0.97$, $p < 0.001$).

Data in (B) and (E) are represented as mean ± SEM. $^{+}p < 0.05$, Wilcoxon Signed rank test. $^{+++}p < 0.001$, Wilcoxon Signed rank test. $^{***}p < 0.001$, Student paired t test.

NVmes, mesencephalic trigeminal nucleus; NVmt, trigeminal motor nucleus; NVsnpr, trigeminal main sensory nucleus; SMOs, subthreshold membrane oscillations.

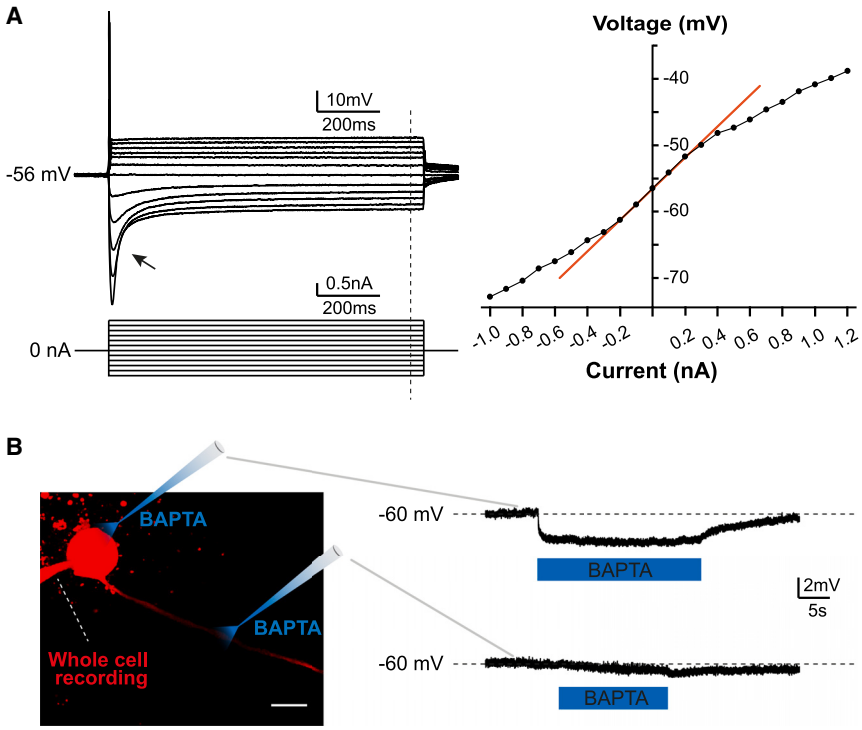

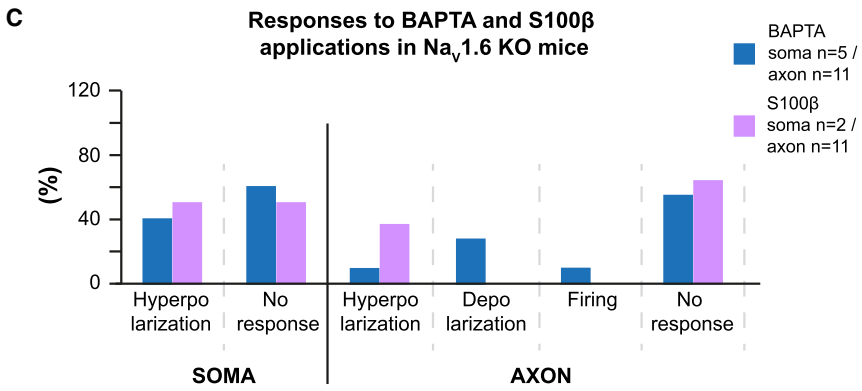

Figure 5. Nav1.6 KO NVmes neurons do not respond to axonal applications of BAPTA and S100β

(A) *Left*: membrane responses of a Na$_V$1.6-KO NVmes neuron (*top* traces) to injections of hyperpolarizing and depolarizing current pulses (*bottom* traces). The arrow points to the sag. The vertical dotted line indicates the position of the membrane voltage and the current injection lecture for the I-V curve. *Right*: I-V curve showing the inward and outward membrane rectification of a spike-adaptative Na$_V$1.6-KO NVmes neuron in response to hyperpolarizing and depolarizing injected current, respectively. The red line is the linear fitting to the non-rectifying portion of the I-V curve.

(B) *Left*: photomicrography of a Na$_V$1.6-KO NVmes neuron filled with intrapipette Alexa 594 with the BAPTA containing micropipette drawn to indicate the positions of the local applications. *Right*: membrane responses of the recorded neuron to somatic (*top* trace) and axonal applications (*bottom* trace).

(C) Bar chart quantifying the response profiles of NVmes neurons to somatic or axonal applications of BAPTA (*blue*), or of S100β (*purple*) in Na$_V$1.6-KO mice. Scale bar: 20 μm.

I-V, current-voltage; KO, knock-out; NVmes, mesencephalic trigeminal nucleus.

this was assessed by making very small and controlled applications of BAPTA or S100β at several locations (1–9) along the length of the axonal process of 34 neurons that were filled with Alexa Fluor 594 or 488 through the patch pipette (as shown in Figure 6A). Great care was taken so that the BAPTA or S100β applied along the single process emerging from the cell body (length 173 ± 34 μm) flew away and not toward the soma. For each of these cases, the exact pipettes position was recorded in bright-field images and drawn offline over the course of the axon (as shown in Figure 6A). In this example, the first application of BAPTA, targeting the soma, produced a hyperpolarizing response (Figure 6A, top trace) while positions 2 and 3 (at 57 and 106 μm from the soma, respectively) produced sustained firing (Figure 6A, 2nd and 3rd traces). BAPTA applications further along the axon had no effects (Figure 6A, bottom traces). A total of 86 applications of BAPTA and S100β were made along the axons of the 34 recorded neurons. The vertical bar chart in Figure 6B illustrates the distribution of responses evoked in relation to the location of the application. Hyperpolarizing responses (gray bars) were mostly elicited by applications less than 40 μm from the soma while firing responses (black bars) were predominantly produced by applications positioned between 40 and 100 μm from the soma. Among the firing responses, those that occurred concomitantly with a membrane potential hyperpolarization (Figure 6C, gray bars) were triggered by more proximal applications, while those accompanied by a depolarizing plateau (Figure 6C, black bars) were elicited by applications at any level of the axon.

Co-localization of Na$_V$1.6 channels and S100β-positive cells and processes around NVmes neurons fibers and somata

The aforementioned data reveal that BAPTA and S100β induce firing in a specific subregion of the axon of NVmes neurons, suggesting that there may be specific sites along the axons of these neurons that are more sensitive to extracellular calcium depletion. Thus, we hypothesized that Na$_V$1.6 and the endogenous calcium chelator S100β may colocalize at these sensitive axonal locations. We used immunohistochemistry to examine the

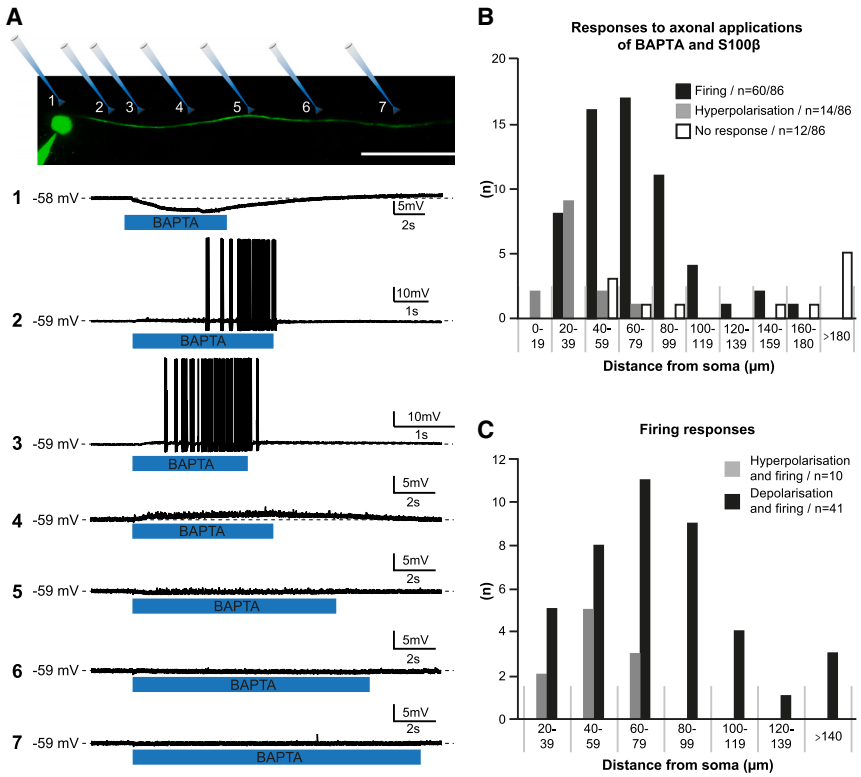

Figure 6. Chelation of extracellular Ca^{2+} around specific axonal subregions initiate NVmes neuronal bursting

(A) *Top*: reconstructed image of the tested NVmes neuron filled with intrapipette Alexa 488, indicating all positions of BAPTA applications along the axon for the recorded membrane responses below. *Bottom 1–7*: electrophysiological responses elicited by local BAPTA applications at the top-illustrated corresponding positions. Somatic application (position 1) of BAPTA induced a hyperpolarization, while bursting was initiated for the 2 and 3 micropipette positions, corresponding respectively to a 57 and 107 μm distance from the soma. Position 4 induced only a slight depolarization associated with membrane potential oscillations, and all further BAPTA applications had no effect. Initial membrane potentials and scale bars are indicated next to each trace.

(B) Bar chart of the distribution of all neuronal responses to the axonal applications of BAPTA and S100β relatively to the distance from the soma of the local application.

(C) Most firing responses were observed following a neuronal depolarization (*black* bars, $n = 41$), but some neurons displayed firing following a hyperpolarization episode (*gray* bars, $n = 10$). Scale bar: 150 μm.

NVmes, mesencephalic trigeminal nucleus.

distribution of S100β-immunoreactive fibers along NVmes neurons' cell bodies and axonal fibers. As many large diameter PAs, NVmes neurons are unipolar and can be positively identified using parvalbumin as in Figure 7A ($n = 6$) that shows them to be surrounded by S100β-immunoreactive cell bodies (arrows) and fibers (arrowheads). Further, combined immunocytochemistry against $Na_V1.6$ channels and S100β showed close apposition of S100β positive processes along $Na_V1.6$ immunoreactive cell bodies and axons of the NVmes neurons in the WT mice ($n = 6$; Figure 7B). Only cell bodies were marked by immunocytochemistry against $Na_V1.6$ in the $Na_V1.6$ null mice ($n = 2$), suggesting that if part of the mutated channel could still be targeted by the antibody, the mutation prevents its successful trafficking to its final position along the axonal process (Figure 7C). Interestingly, NVmes somata are also S100β-immunoreactive. Similar observation was reported in the rat NVmes.[30] A study using single ribonucleic acid (RNA) sequencing revealed that NVmes neurons express S100β,[31] leading us to believe that the labeling observed in the cell bodies of these neurons is not artifactual.

Activation of astrocytes near NVmes neurons axons causes firing

Given that S100β is present in the vicinity of axonal $Na_V1.6$ and because astrocyte activation/depolarization has been linked to astrocyte release of S100β,[21,32] we used mice expressing ChR2 under the astrocytic GFAP promoter to examine the effects of stimulating surrounding astrocytes on NVmes neurons. The recorded neurons were filled with Alexa Fluor 594 through the patch pipette to visualize their cell body and axon and to allow manual delimitation of defined zones for optogenetic stimulation of neighboring astrocytes. Ninety neurons showing a round or ovoid cell body were recorded in the NVmes of 63 GFAP-ChR2 mice. A single process emerging from the cell body could be visualized in 73 of them (length 133 ± 9 μm). Regions of interest (ROIs) were drawn to stimulate the astrocytes around the soma only in 26 neurons (Figure 8A), around the soma and the axonal process in 10 neurons (Figure 8B), and around the axonal process only in 67 neurons (Figure 8C), respectively. The parameters of the photostimulated areas were measured offline for the cases where images were recorded (Table 4). In some cells, more than one neuronal compartment was tested. The recorded neurons showed similar electrophysiological properties to the neurons recorded in WT mice (see Table 1).

Activation of the peri-somatic astrocytes

Optogenetic stimulation of astrocytes in areas encompassing the soma but excluding the axon of the recorded neuron generally led to a small depolarization (Table 5; Figure 8A, top trace; $n = 15$) or no effect ($n = 7$). Other responses observed included biphasic responses consisting of a small long-lasting depolarization followed by a hyperpolarization (Figure 8A, second trace; $n = 2$), or an increase in firing frequency in a cell that was spontaneously firing (not shown). Different stimulation durations were tested (from 10 to 40 s) to see if firing could be elicited, but even though the observed depolarizations outlasted the stimulation period, firing could not be elicited except for the cell that was spontaneously active, and one other cell where a single spike was produced. The size of the stimulated area was measured

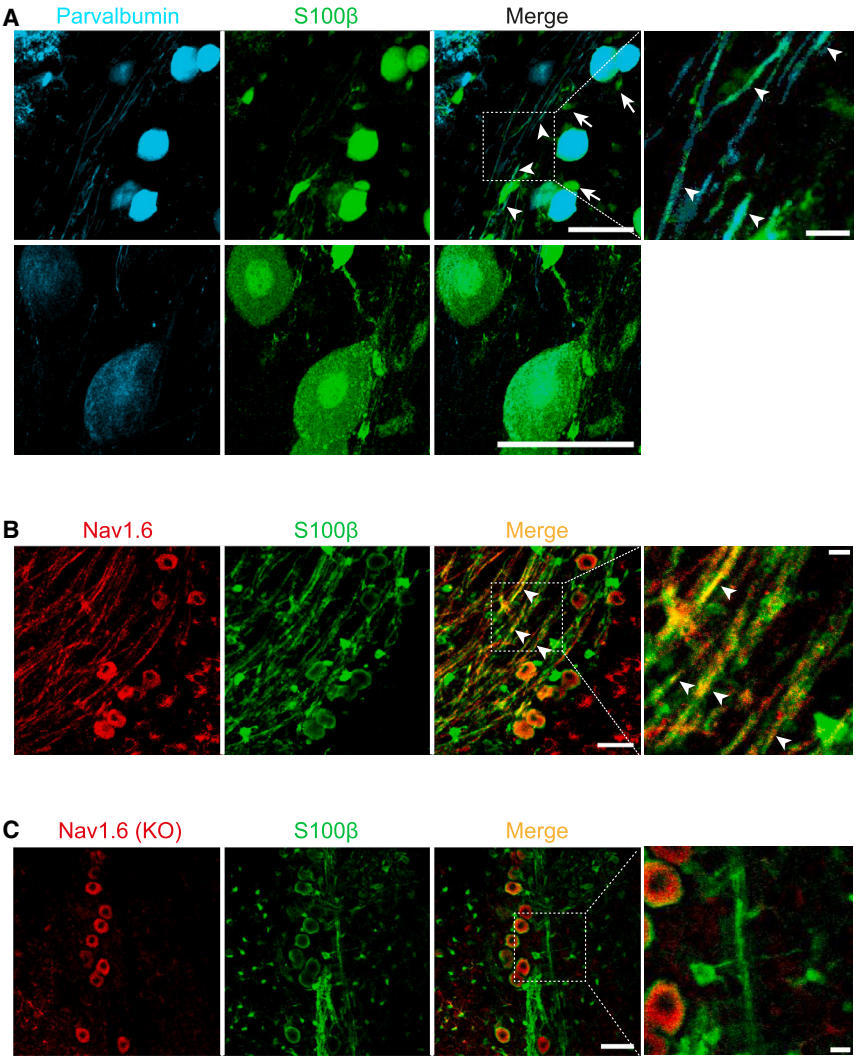

Figure 7. Close relationship between astrocytes and $Na_V1.6$ immuno-positive NVmes neurons

(A) *Top*: parvalbumin-positive NVmes neurons (cyan, *left*) cell bodies are surrounded by astrocytes (arrows) (S100β staining, *second*, green) that also contact NVmes axons (arrowheads). *Bottom*: higher resolution images of parvalbumin-positive NVmes neurons (cyan, *left*) and S100β immunostaining (green, *middle*) that show that NVmes neurons are clearly S100β immuno-positive but that the intensity of the labeling seen in top (*middle*) is due in part to enwrapping of NVmes neurons somata by astrocytic processes.

(B and C) Immunofluorescence staining of Nav1.6 (*left* panels, red), S100β (*second*, green) and superposition of Nav1.6 and S100β (*right*, yellow) in WT (B) and Nav1.6 KO (C) mice. Axonal colocalization of Nav1.6 and S100β indicating axonal apposition of astrocytic processes over Nav1.6 channels (arrowheads) is observed in WT, but not Nav1.6 KO mice.

Scale bars are 10 μm for the zoomed images (fourth images in A [top], B, and C) and 50 μm for the other images. KO, knock-out; NVmes, mesencephalic trigeminal nucleus; WT, wild type.

offline in 20 of the 26 cases where images were recorded (Table 4).

Activation of the astrocytes surrounding the cell body and the axonal process

In 10 cells, stimulation of larger areas that included the soma and the proximal part of the axon also produced long-lasting depolarizations in 8 cases (Table 5; Figure 8B). A volley of 14 action potentials (not shown) was elicited in one case, while no detectable response could be seen in the last tested case. The size of the photostimulated area and the length of exposed axon were measured offline in 6 of the 10 cases where images were recorded (Table 4). The vertical bars chart in Figure 8D illustrates the relative distribution of the different responses elicited by the optogenetic stimulation of the astrocytes surrounding the cell body and the proximal axon (gray bars) of the patched neurons.

Activation of the peri-axonal astrocytes

In 67 of the 90 patched neurons, a ROI drawn for photostimulating the astrocytes excluded the cell body and was restricted to part of the axonal process and the surrounding astrocytes. In some cells, more than one site was tested along the length of the axon and some sites were counted more than once because they were tested with different durations and/or with/without current injection for a total of 111 sites of stimulation (Table 5). The size of the photostimulated area, its distance from the soma, and the length of the exposed axon were measured offline in 93 of the 111 cases where images were recorded (Table 4). As with peri-somatic stimulation, when tested at the RMP, peri-axonal astrocytic optogenetic stimulation produced a long-lasting depolarization (Table 5; Figure 8C, top trace) that outlasted the optogenetic pulse duration for 67 stimulation sites.

Biphasic responses were elicited by stimulating 2 other sites (Table 5, not shown), and firing overriding long-lasting plateaux (Figure 8C, bottom trace) were seen in 11 other neurons (2 of which were spontaneously firing). In the 9 remaining cases, the optogenetic stimulation caused no detectable response.

To facilitate propagation of the stimulation-evoked action potentials into the cell body of the recorded neuron, we tried pairing the optogenetic stimulation of the astrocytes surrounding the axon to membrane depolarization, using current injection, in 22 neurons; 18 of which had been tested at their RMP (-53 ± 1). One neuron did not respond to the optogenetic stimulation while the 17 remaining ones responded with a subthreshold long-lasting depolarization. Injection of depolarizing current (140 ± 16 pA, $n = 22$) brought the membrane potential to -44 ± 1 mV ($n = 22$). In 4 of these, prior depolarization did not change significantly the

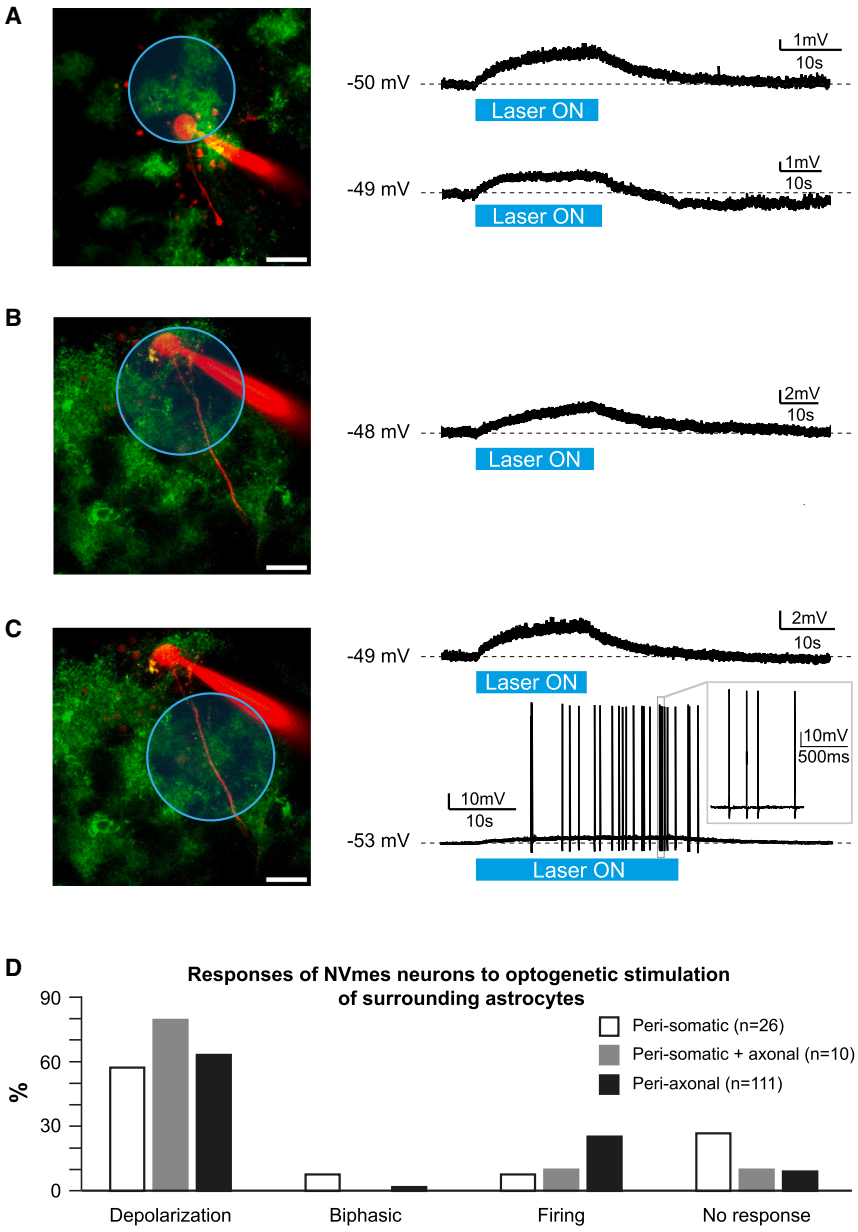

Figure 8. Optogenetic stimulation of peri-neuronal astrocytes in GFAP-ChR2-EYFP mice elicits a diversity of effects

(A–C) Photomicrographs of the area of optogenetic stimulation (*blue* circle) of peri-somatic astrocytes (A), or both peri-somatic and peri-axonal astrocytes (B) or only peri-axonal astrocytes (C) (green astrocytes, red through intrapipette Alexa 594 recorded NVmes neuron). (A) Example of a long-lasting depolarization response (*top* trace) and of a biphasic response consisting of a depolarization followed by a hyperpolarization (*bottom* trace) induced by the optogenetic stimulation of peri-somatic astrocytes. (B) Example of a long-lasting depolarization response induced by the optogenetic stimulation of both peri-somatic and peri-axonal astrocytes. (C) Example of a long-lasting depolarization response (*top* trace) and of repetitive firing (*bottom* trace) induced by the optogenetic stimulation of peri-axonal astrocytes.

(D) Bar chart of the responses of NVmes neurons to optogenetic stimulation of peri-somatic (*white*), peri-somatic and peri-axonal (*gray*) and only peri-axonal (*black*) astrocytes. Scale bars: 50 μm.

ChR2, channelrhodopsin 2; EYFP, enhanced yellow fluorescent protein; GFAP, glial fibrillary acidic protein; NVmes, mesencephalic trigeminal nucleus.

amplitude (paired t test, $p = 0.281$), the latency (paired t test, $p = 0.422$), or the duration (paired t test, $p = 0.901$) of the depolarization induced by astrocytic stimulation (Table 5). The non-responding neuron still failed to respond with prior depolarization. For 17 neurons, the pairing of the optogenetic stimulation of peri-axonal astrocytes with depolarizing current injection (which caused some firing by itself in 2/17 cases) triggered sustained firing overriding the long-lasting depolarizing plateau (as in Figure 8C, bottom trace). The vertical bars chart in Figure 8D illustrates the relative distribution of the different responses elicited by the optogenetic stimulation of the astrocytes surrounding the axon (black bars) of the patched neurons.

In summary, the optogenetic stimulation of peri-axonal astrocytes (tested in a total of 111 peri-axonal sites in 67 NVmes neurons) caused ($n = 24$) or increased ($n = 4$; Student paired t test, $p = 0.03$) firing in 28 cases. As with the local applications of BAPTA and S100β, different firing patterns were observed in response to the stimulation of the peri-axonal astrocytes. The most prevalent pattern seen in 11 cases was bursting with the emission of a single burst 9 and 13 s after the start of the stimulation in 2 cases and repetitive bursting in the other 9 cases (Figure 9A, top trace; latency of 6 ± 1; duration of 16 ± 3 s; interburst frequency: 1 ± 0.3 Hz; intra-burst frequency: 65 ± 4 Hz). In one case, a single spike was elicited at a latency of 9.2 s while in 7 cases, low-frequency train of singlets was induced (Figure 9A, second trace; frequency 0.8 ± 0.2 Hz; latency: 6.4 ± 1 s; duration: 30 ± 14 s). High frequency (89 Hz) train intermingled with bursting (Figure 9A, third trace) was seen in a single cell, while 8 stimulations gave rise to a mix of low-frequency train of singlets and bursts (latency: 3 ± 0.3 s; duration: 17 ± 5 s) (Figure 9A, bottom trace). The vertical bars chart in Figure 9B illustrates the relative distribution of the different firing patterns observed in response to the optogenetic stimulation of the peri-axonal astrocytes while Figure 9C illustrates the distribution of these 28 firing responses among the 3 types of recorded NVmes neurons.

Interestingly, in 19 cases, optogenetic stimulation of peri-axonal astrocytes caused an increase of the amplitude (1.7 ± 0.1 mV vs. 2.4 ± 0.2 mV, Wilcoxon Signed-rank test, $p < 0.001$)

Table 4. Stimulated areas

	Surface (μm2)	Distance from the soma (μm)	Length along the axon (μm)
Peri-somatic	8,240 ± 2,227 *n* = 20	Soma included	0
Peri-somatic + axonal	23,439 ± 6,940 *n* = 6	Soma included	89 ± 21
Peri-axonal	8,589 ± 585 *n* = 93	52 ± 4	65 ± 4

Values are mean ± SEM.
n = number of images analyzed.

and a decrease of the frequency (74 ± 6 Hz vs. 61 ± 4 Hz, paired t test, $p = 0.041$) of the SMOs. The optogenetic stimulation of peri-axonal astrocytes also triggered firing at slightly more hyperpolarized potentials than did standard step current injections (−45 ± 1 mV vs. −47 ± 1 mV, paired t test, $p = 0.002$, $n = 10$) in 10 of the 11 neurons in which spikes were elicited at RMP.

A precise axonal subregion is involved in the astrocytes-induced firing

We then sought to examine, using the images recorded for offline analysis, if, as with axonal applications of BAPTA and S100β, a specific subregion could be identified along the axonal process of the recorded neurons for the successful triggering of firing with optogenetic stimulation of peri-axonal astrocytes. We drew horizontal lines (blue, cyan, black, and gray lines in Figures 10A–10D) along the axon of a schematic illustration of an NVmes sensory neuron (red pseudo-unipolar cells in Figures 10A–10D) representing the length and distance from the soma of the portion of illuminated axon for each trial of optogenetic stimulation of peri-axonal astrocytes for 3 categories of evoked responses and for the cases where no responses could be detected. It appears that, without the aid of imposed depolarization, the firing responses ($n = 11$, Figure 10A) were predominantly evoked by stimulation zones that cover the portion of the axon comprised between 25 and 80 μm from the soma. Membrane depolarization extends the length of the responsive axon proximally relatively to the soma ($n = 14$, Figure 10B). Long-lasting depolarizations could be elicited at all levels of the axon length ($n = 58$, Figure 10C) while the cases of failures to respond are evenly distributed along the axonal length ($n = 10$, Figure 10D). Those observations are summarized in the bar chart in Figure 10E, which represents the responses evoked by the optogenetic stimulation of peri-axonal astrocytes in relation to the position of the proximal extremity of the covered area of stimulation.

The astrocytes-induced firing depends on S100β and $Na_v1.6$ channels

To elucidate whether release of endogenous S100β in the extracellular space was involved in the observed effects, we tested whether local applications of an anti-S100β antibody (40–80 μg/mL) affected firing induced by optogenetic stimulation of neighboring astrocytes. Figure 11A (*top* trace) illustrates the response evoked in the patched neuron shown in

Table 5. Effects of optogenetic stimulation of astrocytes on NVmes neurons

		Depolarization			Firing			
		Latency (s)	Amplitude (mV)	Duration (s)	Latency (s)	Duration (s)	Biphasic	No effect
Peri-somatic (10–40 s) *n* = 26/*N* = 26	At RMP	0.4 ± 0.1 (*n* = 15) *N* = 15	2 ± 0.2	17–77	17 and 2.2 (*n* = 2) *N* = 2	0.03 and 28	(*n* = 2) *N* = 2 Lat.3.2 and 0.9 s	*n* = 7 *N* = 7
Peri-somatic + peri-axonal (30 s) *n* = 10/*N* = 10	At RMP	0.6 ± 0.1 (*n* = 8) *N* = 8	1.7 ± 0.4	50 ± 7	14 (*n* = 1) *N* = 1	14	_	*n* = 1 *N* = 1
Peri-axonal (5–30 s) *n* = 111/*N* = 67	At RMP *n* = 89/*N* = 64	0.5 ± 0.1 (*n* = 67) *N* = 51	1.7 ± 0.1	14–114	6.5 ± 1.1 (*n* = 11) *N* = 10	0.03–112	(*n* = 2) *N* = 2 Lat. 0.3 and 0.7 s	*n* = 9 *N* = 7
	With depolarizing current *n* = 22/*N* = 22	0.7 ± 0.4[a] (*n* = 4) *N* = 4	2.5 ± 1[b]	21–73[c]	5.1 ± 0.5 (*n* = 17) *N* = 17	47 ± 11	_	*n* = 1 *N* = 1

Values are mean ± SEM for data that can be averaged; exact values for $n < 3$; or intervals for duration data acquired with different stimulation durations. Lat., latency; *n*, number of stimulation sites; *N*, number of neurons; (*n*), number of responses; NVmes, mesencephalic trigeminal nucleus; RMP, resting membrane potential.
[a]Value not different from control for the 4 depolarizations tested at RMP; control latency, 0.5 ± 0.2 s, paired t test, $p = 0.422$.
[b]Value not different from control for the 4 depolarizations tested at RMP; control amplitude, 2.8 ± 1.9 mV, paired t test, $p = 0.281$.
[c]Value not different from control for the 4 depolarizations tested at RMP: control duration, 46 ± 19 s, paired t test, $p = 0.91$.

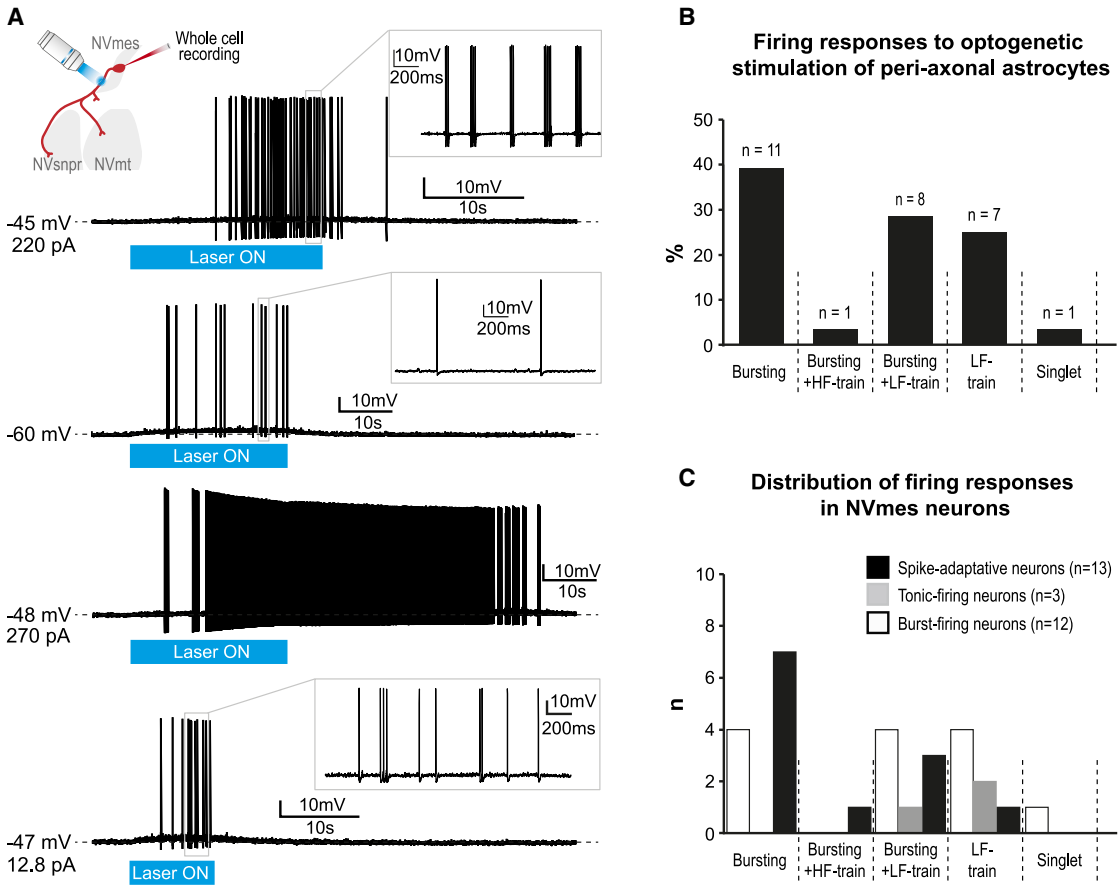

Figure 9. NVmes neurons firing responses to the optogenetic stimulation of peri-axonal astrocytes in GFAP-ChR2-EYFP mice

(A) The optogenetic stimulation (blue light, combination of 440 and 488 nm lasers, 15% laser power) of peri-axonal astrocytes (as illustrated by the cartoon) triggered diverse firing patterns in the recorded NVmes neurons including bursting (*top* trace), low-frequency train of action potentials (*second* trace), bursting associated with high- and low-frequency train of action potentials (*third and bottom* traces, respectively).

(B) Bar chart of the relative distribution of the firing responses (shown in A) elicited by peri-axonal astrocytes stimulations.

(C) Bar chart of the relative distribution of the neuronal firing responses elicited by peri-axonal astrocytes stimulations in the spike-adaptative (black bars), tonic-firing (gray bars), and burst-firing (empty bars) NVmes neurons.

ChR2, channelrhodopsin 2; EYFP, enhanced yellow fluorescent protein; GFAP, glial fibrillary acidic protein; HF, high-frequency; LF, low-frequency; NVmes, mesencephalic trigeminal nucleus; NVmt, trigeminal motor nucleus; NVsnpr, trigeminal main sensory nucleus.

the image by the optogenetic stimulation of the astrocytes (arrowheads) enclosed in the delineated zone (blue circle) around its axon. Local application of the S100β-subunit monoclonal antibody completely abolished the firing (Figure 11A, *middle* trace**;** *n* = 5 neurons, from 5 slices, from 5 animals) induced by the optogenetic stimulation that gradually recovered (Figure 11A, *bottom* trace) after washout of the antibody. However, the small-amplitude underlying depolarizations remained in the presence of the anti-S100β antibody in the 5 tested cases (Figure 11A *middle*, top trace above the dotted baseline in inset).

To further determine if the effect of endogenous S100β also involved $Na_V1.6$ channels, we tested the effect of bath-applications of 4,9-anhydro-TTX on the astrocytes-induced firing in 2 neurons (from 2 slices, from 2 animals). Figure 11B (*top* trace) illustrates the response evoked in one of these neurons by the optogenetic stimulation of the astrocytes surrounding its axon. Bath-application of 4,9-anhydro-TTX completely abolished the firing (Figure 11B, *middle* trace) induced by the optogenetic stimulation that recovered (Figure 11B, *bottom* trace) after the washout of the drug. Again, the small-amplitude underlying depolarizations remained in the presence of the 4,9-anhydro-TTX in the 2 tested cases (Figure 11B, *middle*, top trace above the dotted baseline in inset).

DISCUSSION

The presented results provide evidence that astrocytes may regulate the excitability and firing patterns of PA neurons in the trigeminal mesencephalic nucleus (NVmes). This regulation is mediated by a local astrocytic release of S100β along a specific axonal domain of NVmes neurons and the subsequent decrease of the extracellular calcium concentration ($[Ca^{2+}]_e$), causing I_{NaP} potentiation and repetitive firing.

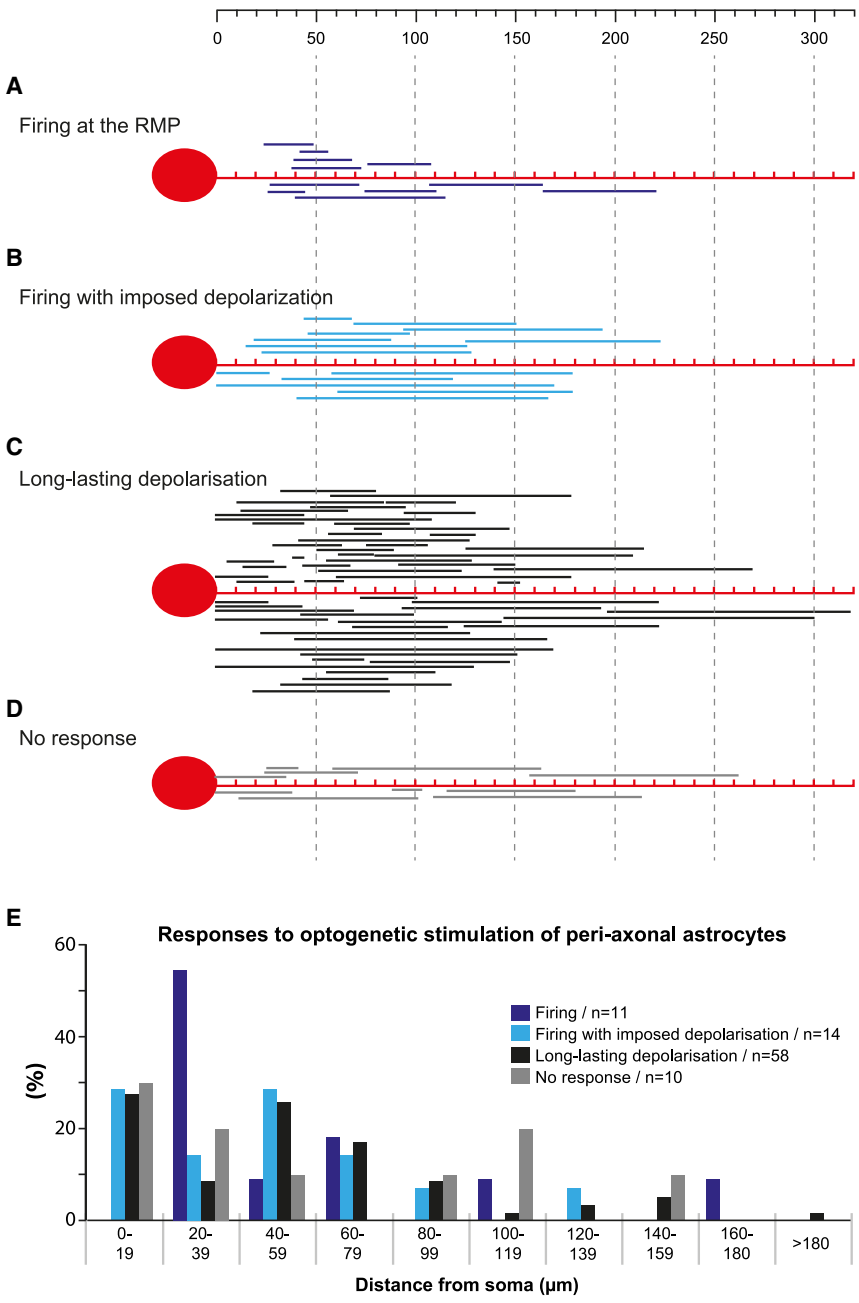

Figure 10. NVmes neuronal firing is initiated by optogenetic stimulation of peri-axonal astrocytes in GFAP-ChR2-EYFP mice surrounding specific axonal subregions

(A–D) Graphic summary of recorded responses following optogenetic stimulations of astrocytes surrounding NVmes axonal subregions in GFAP-ChR2-EYFP mice in relation to the position of the proximal extremity of the covered area of stimulation from 0 to 300 μm of distance from the soma (top grid lines) for 93 of the 111 stimulation sites where images were recorded for offline analysis.

(E) All responses with the nominal distances of the proximal extremity of the covered area from the soma are plotted.

Following these optogenetic stimulations, we observed firing at the resting membrane potential for 11 stimulation sites (A; E purple bars) and firing following an imposed depolarization for 14 stimulation sites (B; E blue bars). The most common response was a long-lasting depolarization elicited by 58 stimulation sites (C; E black bars), with 10 sites producing no response (D; E gray bars).

ChR2, channelrhodopsin 2; EYFP, enhanced yellow fluorescent protein; GFAP, glial fibrillary acidic protein; NVmes, mesencephalic trigeminal nucleus; RMP, resting membrane potential.

Ionic conductances contributing to NVmes neurons properties and firing and their modulation by Ca^{2+}-chelating agents

The recorded neurons exhibited the distinctive electrophysiological properties and unipolar morphology of PAs[33] previously described in the rat or mouse NVmes (for review, see study by Xing et al.[34]). The vast majority (75%) of them showed firing accommodation upon membrane depolarization. This property, which relies on a 4-aminopyridine-sensitive (4-AP-sensitive) outward potassic current,[35] has been shown to be more prevalent in mouse than in rat NVmes neurons due to a significantly higher magnitude of the D-type K^+ current.[36] Interestingly, S100β has recently been reported to inhibit A-type voltage-gated and EAG1 K^+ channels.[37] Inhibition of these channels could contribute to the observed increase in firing, but this is unlikely the case here because these firings were not seen in the Nav1.6 KO and were abolished by 4,9-TTX. In addition, according to Saito et al.,[38] the 4-AP- K^+ channels are located exclusively on the somata of NVmes neurons, where Ca^{2+} chelation caused a hyperpolarization rather than an increase in firing. This hyperpolarization may reflect the effect of Ca^{2+} decrease on a variety of channels, sensors, exchangers, and receptors, but may also result from the fact that lower Ca^{2+} may activates astrocytes and lead to release of adenosine triphosphate and/or a transient decrease in the extracellular K^+ concentration.[39]

In the remaining 25% of neurons reported here, repetitive firing and SMOs were observed upon membrane depolarization. Such SMOs and firing were also obtained in more than half of the spike-adaptative neurons with local applications of BAPTA or S100β, at some point along their axonal process. SMOs and repetitive firing depend on a I_{NaP}[8–10,12] conveyed in NVmes neurons by the $Na_V1.6$ channel isoform[25] that is highly sensitive to $[Ca^{2+}]_e$. By entering and clogging the pore of the channel, Ca^{2+} reduces the current by interfering with the flow of Na^+ ions,

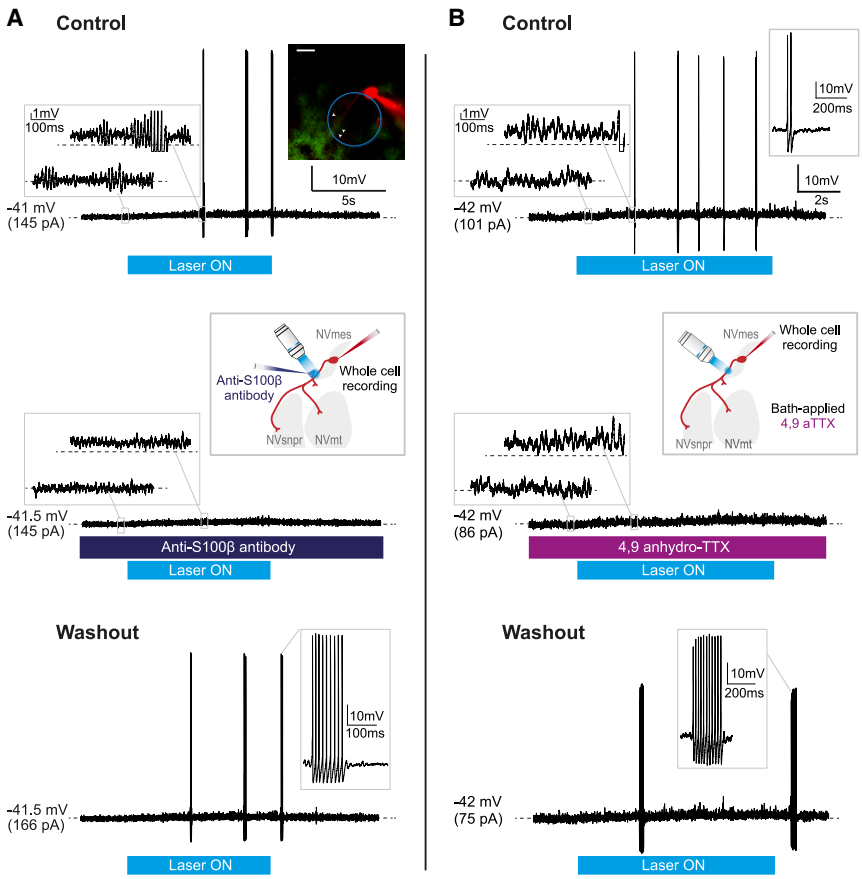

Figure 11. Firing triggered in NVmes neurons by optogenetic stimulation of peri-axonal astrocytes in GFAP-ChR2-EYFP mice is reversibly suppressed by the application of an S100β antibody and a $Na_V1.6$ channel blocker

(A) Transient bursting (*top* trace; left inset emphasizes the slight depolarization underlying the firing**)** induced in an NVmes neuron by a 10 s optogenetic stimulation of its peri-axonal astrocytes (arrowheads in blue circle in photomicrograph) is abolished following local application of the anti-S100β antibody (*middle*; left inset emphasizes the remaining slight depolarization, right inset illustrates the experimental setup**)** and recovered after a 35-min wash (*bottom*).

(B) Doublets and singlets (*top* trace; left inset emphasizes the slight depolarization underlying the firing) induced in an NVmes neuron by a 10 s optogenetic stimulation of its peri-axonal astrocytes are abolished following the addition of 4.9-anhydro-TTX, a selective Nav1.6 antagonist, to the perfusion bath (*middle*; left inset emphasizes the remaining slight depolarization, right inset illustrates the experimental setup). *Bottom*: a bursting response was recovered after a prolonged wash. Scale bar: 50 μm.

ChR2, channelrhodopsin 2; EYFP, enhanced yellow fluorescent protein; GFAP, glial fibrillary acidic protein; NVmes, mesencephalic trigeminal nucleus; NVmt, trigeminal motor nucleus; NVsnpr, trigeminal main sensory nucleus.

and modifies the voltage-sensitivity and gating kinetics of the channel.[19] As a consequence, calcium-chelating agents, such as BAPTA and S100β, augment the amplitude and duration of $I_{NaP,}$ thereby increasing the occurrence of SMOs and repetitive firing. Indeed, our previous work showed, using voltage-clamp recordings in NVsnpr neurons, that both substances increase the peak amplitude of the pharmacologically isolated I_{NaP} and shift its activation and half-activation voltage toward more hyperpolarized potentials.[20] The transition from adaptative to bursting-firing neurons with BAPTA and S100β is in agreement with Yang et al.[23] who showed that NVmes neurons excitability could be transformed from one class to another by manipulating the magnitude of $I_{4\text{-}AP}$ and/or I_{NaP}. This is also supported by the observation that NVmes neurons in our $Na_V1.6$ knockout mice were less excitable than the ones from the WT mice since almost all (93%) of them showed firing accommodation and a depolarized firing threshold (relatively to WT NVmes neurons), as reported by others.[25,40,41]

$[Ca^{2+}]_e$ chelation along a precise segment of NVmes neurons axonal processes elicits repetitive firing

As in the study of Chung et al.,[42] our immunohistochemical data showed immunoreactivity against $Na_V1.6$ channels in NVmes neurons somata and along their axon. However, the somatic labeling, which was weak, could be detected only in the cytoplasm but not at the membrane, suggesting absence of these channels on the soma membrane. This is in agreement with the findings of Kang et al.[43] who, on the basis of dual patch recordings from the soma and axon hillock of NVmes neurons, concluded using pharmacological tools that the two compartments express different Na^+ channels and that I_{NaP} is likely present solely in the stem axon. This could explain why there was no increase in excitability in the recorded neurons, in our study, when BAPTA and S100β were applied near their soma, while their applications near the axonal process elicited firing in 80% of cells which were mostly quiescent priorly. The elicited firing showed a significantly more hyperpolarized threshold potential than the firing evoked by standard step current injection that activates voltage-gated Na^+ transient channels, suggesting that it is likely generated via $Na_V1.6$ channels in which voltage-dependence activation occurs at more hyperpolarized potentials than other neuronal Na_Vs channels[44,45] (reviewed in a study by Zybura et al.[46]). Accordingly, these firings were prevented with the selective blockade of $Na_V1.6$ channels with 4,9-TTX and could not be elicited in $Na_V1.6$ null mice (except in 1 out of 22 applications) where our immunohistochemical data confirmed absence of $Na_V1.6$ channels on the axons. The immunopositivity to $Na_V1.6$ in NVmes neurons somata of $Na_V1.6$ knock-out mice can be explained by the antibody targeting an intracellular loop (between domains II and III) of the sodium channel α subunit unaltered by the med mutation, which truncates the protein within the first transmembrane domain.[29] Our immunohistochemical

results in the $Na_V1.6$ null mice suggest that the channel encoded by the mutated gene is not transported to the axon, as it has been reported by others.[47]

In neurons, $Na_V1.6$ channels localize mostly in the distal end of the AIS[17] and are presumed to be responsible for the action potential initiation.[48,49] The AIS as defined by marking of ankyrin G (AnkG) that anchors Na^+ in the spike initiation zone is usually located close to the soma of central neurons,[50] but PAs may also have spike initiation zones in their peripheral branches near their receptor in the periphery. For instance, Espino et al.[51] found that muscle spindles possess several action potential initiation zones co-expressing $Na_V1.6$-expressing and AnkG with some being close to the spindle capsule. Nascimento et al.[52] reported that in the dorsal root ganglia (DRG) TrkC-positive proprioceptive neurons, which are equivalent to NVmes neurons, a 50–60 μm long initial segment, starting at 12 μm from the soma, could be observed in 25%–30% of neurons. Considering this and the fact that the $Na_V1.6$ channels are absent in the more proximal part of the AIS,[17] it is interesting that firing responses elicited with axonal applications of the Ca^{2+}-chelating agents that did not require facilitating depolarization were elicited with applications distanced 20–80 μm from the soma.

Chung et al.[42] reported co-localization of mGluR-I receptors with $Na_V1.6$ channels on the stem axon of NVmes neurons, suggesting that glutamatergic synaptic action at this location upregulates I_{NaP} to trigger bursts, providing a complementary firing mechanism. However, as no synaptic stimulation was applied in our study and no spontaneous firing was observed, the evoked firings likely resulted from a direct effect of punctual decreases of extracellular calcium on I_{NaP} along NVmes neurons axons. mGluR-I receptors may still explain the small depolarization persisting after blockade of induced firing with 4,9-TTX and/or anti-S100β antibody, and could also underlie the increased SMOs and firings reported by Verdier et al.[53] after stimulating surrounding trigeminal areas.

Activation of astrocytes closely apposed to NVmes axonal processes leads to ectopic firing through the release of S100β

In the periphery, satellite glial cells, which are the equivalent counterparts to the astrocytic glial cells of the central nervous system, closely envelop the cell bodies of the sensory neurons located within the DRG and trigeminal ganglia (TG), utterly isolating them from each other (reviewed in studies by Hanani and Spray[54] and Zheng et al.[55]). It was speculated that this peculiar organization allows for close interactions between satellite glial cells (SGCs) and neurons[56] and emphasizes the absolute control these glial cells can exert over the extracellular milieu that surrounds these sensory neurons. Our immunohistochemical data reveal that although NVmes PAs are not as tightly enveloped by S100β-positive glial processes as DRG neurons, they are still well surrounded. S100β-positive glial cell bodies and processes are seen closely surrounding the somata and axons of these cells. However, the morphological relationship between astrocytes and NVmes neurons somata may be underestimated in our study because of our choice of astrocytic marker, since S100β mostly labels astrocytic cell bodies and proximal astrocytic processes. Using anti-GFAP antibodies in a study conducted on rats, Copray et al.[57] reported that each NVmes neuron was almost entirely sheathed with astrocytic processes radiating out from two or more astrocytes. Such anatomical organization places astrocytes in a strategic position to tightly regulate the excitability of the NVmes sensory neurons in the same way as the SGCs of the DRG and TG.

Within the ganglia, the gap of extracellular space between the SGC sheath and the wrapped neuronal surface has a very constant distance of about 20 nm, comparable to the distance found in a synaptic cleft (reviewed in the study by Zheng et al.[55]). Given how narrow that space is, a change of just a few ions will cause significant variation in its concentration and have a major effect on phenomena that depend on it,[58,59] as previously suggested and modeled by Smith SJ.[59] If such a small distance is found between astrocytic processes and NVmes neurons axonal membrane, as suggested by their close apposition in our immunohistochemical data, then the release of even a minute amount of S100β in such a confined space would produce a significant decrease of $[Ca^{2+}]_e$ and powerfully activate $Na_V1.6$ channels leading to facilitation of firing and its propagation. This could even be responsible for ectopic discharges that are sometimes seen in pathological pain states.[60–63]

Optogenetic activation of astrocytes via the expression of channelrhodopsin has been used by many and was shown to elicit intracellular calcium rises and to lead to the release of several gliotransmitters.[21,64–71] The specificity of the channelrhodopsin expression and the efficacity of the optogenetic stimulation on the illuminated astrocytes in the GFAP-ChR2 mice used in the present study have already been established in our more recently published work.[21] Here, using this mouse line, we found that photostimulation of astrocytes surrounding the axon of NVmes neurons elicited firing that, as those evoked by local applications of BAPTA or S100β, relied on the activation of I_{NaP} and showed a significantly more hyperpolarized threshold potential than the firing evoked by current injection, suggesting that they may result from the release of S100β. Indeed, these firings could be reversibly blocked by application of an anti-S100β antibody. We did not test the effect of astrocytic photostimulation on $[Ca^{2+}]_e$, but according to Ryzcko et al.,[21] such stimulation in the layer 5 of the visual cortex was associated with a drop of 0.13 mM. That a detectable drop could be recorded in a submerged preparation, continuously perfused with a calcium-loaded artificial cerebrospinal fluid (aCSF), is somewhat remarkable and we would presume that the calcium drop was likely greatly underestimated particularly in the extracellular space in area of close apposition between glial processes and neuronal membrane.

Photostimulation of NVmes astrocytes contributes to augmented neuronal excitability by amplifying SMOs and generation of ectopic repetitive firing that both rely on I_{NaP}. The unique pseudounipolar morphology of these centrally located neurons points to this regulatory effect of astrocytes taking place along the axonal process and adds to the accumulating evidence that these glial cells interfere with signal processing at all levels of the input-output computation within neuronal circuits. Involvement of I_{NaP} in distal axon excitability has already been

demonstrated in CA1 pyramidal neurons,[72] but the present study extends this demonstration by revealing that astrocytes, through the release of S100β along axonal process, act as key regulators of I_{NaP}.

Functional considerations

Synchronization and signal amplification

NVmes neurons are known to be electrically coupled through connexin 36 (Cx36) gap junctions,[36,73–75] but coupling is mostly restricted to pairs or small clusters.[74] Curti et al.[74] found this coupling to strongly promote robust spike synchrony among pairs of afferent neurons through a synergistic interaction with active membrane properties but attributed its strength to only a small fraction of the Cx36 channels. Based on the lack of tracer-coupling (estimated with neurobiotin injections and Cx36 labeling), they suggested that most channels are closed and must be strongly regulated. Indeed, coupling between cells is dynamic and can be up or downregulated. $[Ca^{2+}]_e$ is one of the factors that can greatly influence gap-junction coupling.[76] Therefore, even if NVmes neurons cell bodies lack I_{NaP}, S100β released by surrounding astrocytes may contribute to an increased excitability and synchronized firing by allowing the transfer of antidromic action potentials along the axon to numerous cells through upregulation of gap-junction coupling. This astrocytic control of coupling is of particular interest in a nucleus where the cells are majorly refractory to discharge, since it may allow to bypass these neurons refractory nature by coupling more excitable cells to the refractory ones. In our study, 43% of the recorded neurons fired a single action potential in response to 1 s long depolarizing pulses current injection probably due to a high expression of a 4-AP-sensitive outward K^+ as previously reported.[38] However, action potentials ectopically generated in the axon are likely to invade the soma and release the strong inhibitory control exerted by this conductance. Davoine and Curti[77] proposed that the reciprocal interaction between active electrical properties and electrical coupling endows circuits of coupled neurons with the capability to act as coincidence detectors and since astrocytes act on both parameters, we propose that they may play an important role in this neuronal function as well.

Lastly, independently of the coupling between NVmes neurons, it is known that a single astrocyte, because of its highly ramified morphology, contacts several cells simultaneously. Thus, a concerted action of a single astrocyte on adjacent axons may suffice to elicit a synchronized activity between many neighboring cells. Debanne and Rama[78] postulated that since a single astrocyte covers a spherical volume with a diameter of ~40 μm, the activity of an astrocyte may affect a large population of axons, creating volumes of enhanced synaptic transmission. Adding that several astrocytes can couple together[79] elevates their influence to another level, and gives a glimpse of the powerful control they may exert on the coordination of firing across neuronal networks.

Neuronal compartmentalization

Our much earlier *in vivo* work in the rabbit[80] suggested that propagation of action potentials is compartmentalized in NVmes neurons during fictive mastication, because antidromic action potentials generated in their central axons during the jaw-closing phase of the masticatory cycle could not be detected in the soma and stem axon area. We postulated then that this allowed some branches of the central axon to act as premotor interneuron, functionally disconnected from the stem axon and soma. At the time, the antidromic action potentials were imputed to strong GABA-mediated PAs depolarizations and regulation of their propagation was thought to rely on activation of GABAergic receptors at strategic locations along the axonal tree.[81,82] While this may be true, contribution of astrocytes, through release of S100β or GABA as previously described[83] also needs to be considered.

Pathologies

Increasing evidence suggest that the SGCs in DRG are activated in chronic pain conditions (reviewed in the study by Zheng et al.[55]) and our own previous work has shown that NVmes astrocytes become reactive in the acidic saline masseteric myalgia model,[84] in which NVmes neurons showed increased excitability.[22] Reactive astrocytes are known to release increased amounts of gliotransmitters.[85] With regard to S100β, it has been shown that its mRNA and protein levels increase in the spinal cord after peripheral inflammation and nerve injury,[86] and in serum in diverse chronic pain conditions.[87–89] It is therefore possible that reactive astrocytes contribute to the increased excitability of NVmes neurons in the chronic myalgia model by releasing excessive amounts of S100β. This mechanism may be at play in any pathology where neuronal hyperexcitability or hypersynchrony is reported.

Concluding remarks

Others have reported regulation of axonal excitability by astrocytes directly, through purinergic[90] and glutamatergic[91] signaling, or indirectly, by acting on the myelin.[92] It therefore appears that astrocytes have a variety of mechanisms at their disposal to impact the electrical properties of axons. In this study, we showed how astrocytes, by releasing S100β in the vicinity of a specific segment of the axonal process of NVmes neurons, modulate their excitability by acting on I_{NaP}. These very peculiar sensory neurons have classically been associated with chewing, an essential rhythmic behavior sustained by an extensive brain circuit (reviewed in a study by Falardeau et al.[93]). However, there is accumulating evidence that their functions go beyond the relaying of jaw proprioceptive inputs for oro-sensory-motor control. Indeed, those cells are involved in numerous other brain functions, such as whisker pad proprioception,[94,95] food intake regulation,[96] stress-induced masseter hyperactivity,[97] and sleep physiology,[98] to name a few. This implies that understanding the factors that regulate their excitability is paramount. The present study underlines the importance in considering the contribution of astrocytes to the basic neuronal computations in this and presumably other circuits.

Limitations of the study

(1) Unspecific effects of local applications of BAPTA, S100β or the anti-S100β antibody. To rule out effects that could result from mechanical disturbance, we tested local applications of aCSF along the axon of five NVmes neurons and found no effects on the recorded cells. In one of these cases, puffing of aCSF at several positions along the axon

of the recorded neuron had no effect; puffing of BAPTA at the same positions elicited firing (Figure S1). We also analyzed the effects of the anti-S100β antibody on the basic electrophysiological properties of NVmes neurons and found no differences before and after its application (Table S1).

(2) Issues related to the use of optogenetic stimulation include: (i) potential expression of ChR2 in NVmes neurons themselves; (ii) the effects of ChR2 on pH and extracellular K^{+}[99]; and (iii) the effects of blue light (high energy) on the tissue.[100]

Regarding the first issue, we first confirmed using immunohistochemistry against the green fluorescent protein and Parvalbumin in GFAP-ChR2-EYFP mice (Figure S2, *bottom*, $n = 3$), that there was no overlap in labeling in the cell bodies of NVmes neurons. Secondly, we tested direct activation of NVmes neurons with optogenetic stimulation in Parvalbumin-ChR2 mice (Figure S3, $n = 8$) and found the main effect to be only depolarizations or firing of one or two spike(s) (Figure S3C), even with prolonged stimulation. In 2 of the 8 cells where such a stimulation failed to induce prolonged firing, further application of S100β induced prolonged firing.

As for the 2nd issue, we reasoned that the firing elicited by optogenetic stimulation of astrocytes is unlikely to result from the release of other factors (due to acidification leading to vesicle fusion) because it is abolished by prior application of the anti-S100β antibody. However, the depolarization that persists in this condition may well reflect effects on extracellular K^{+}.

The 3rd issue was addressed in two series of control experiments. First, in GFAP-ChR2-EYFP mice, no effects were elicited in NVmes neurons upon optogenetic stimulation in cases where there were no labeled astrocytes in the vicinity of the recorded cell (Figure S4A, $n = 5$). In the second series of experiments, conducted on brainstem slices from GFAP-cre mice, astrocytes (not expressing ChR2) were first marked with Sulforhodamine-101 (Figure S4B, in red) to identify their presence and stimulated with blue light with the same laser intensity used in the experiments conducted on brainstem slices from GFAP-ChR2-EYFP mice. No effects were observed on the recorded NVmes neuron (Figure S4B, $n = 7$), while BAPTA application induced firing (Figure S4C).

(3) Presence of S100β in large PAs has previously been described, but it is unclear whether it results from expression of the protein in the afferents or its uptake from the extracellular space.[101–103] This makes it difficult to ascertain that the observed effects result from its astrocytic release. However, it is unlikely to result from its neuronal release since direct optogenetic stimulation of NVmes neurons in Parvalbumin-ChR2 mice did not elicit sustained firing.

RESOURCE AVAILABILITY

Lead contact

Further information and requests for resources and reagents should be directed to and will be fulfilled by the lead contact, Arlette Kolta (arlette.kolta@umontreal.ca).

Materials availability

This study did not generate any new unique reagents.

Data and code availability

- All data reported in this paper will be shared by the lead contact upon request.
- This paper does not report original code.
- Any additional information required to reanalyze the data reported in this paper is available from the lead contact upon request.

ACKNOWLEDGMENTS

Rafael Sanz-Gálvez generously performed the immunostaining of S100β and Parvalbumin in the NVmes. Reza Sharif-Naeini graciously supplied the Pvalb-cre-tdTomato mice. This work was supported by the Canadian Institutes of Health Research (#165900).

AUTHOR CONTRIBUTIONS

Conceptualization, P.M. and A.K.; methodology, P.M., J.G., F.G., and M.C.-L.; investigation, J.G., F.G., and M.C.-L.; validation, J.G., F.G., D.V., and A.K.; formal analysis, J.G., F.G., and D.V.; visualization, J.G., F.G., and D.V.; supervision, P.M., D.V., and A.K.; writing – original draft, J.G., F.G., and D.V.; writing – review and editing, P.M. and A.K.; funding acquisition, A.K.; resources, A.K.

DECLARATION OF INTERESTS

The authors declare competing interests.

STAR★METHODS

Detailed methods are provided in the online version of this paper and include the following:

- KEY RESOURCES TABLE
- EXPERIMENTAL MODEL AND STUDY PARTICIPANT DETAILS
- METHOD DETAILS
  - Brainstem slice preparation
  - Electrophysiology and analysis
  - Optogenetic stimulation
  - Drug application
  - Immunohistochemistry
- QUANTIFICATION AND STATISTICAL ANALYSIS

SUPPLEMENTAL INFORMATION

Supplemental information can be found online at https://doi.org/10.1016/j.isci.2025.112006.

Received: August 30, 2024
Revised: December 31, 2024
Accepted: February 10, 2025
Published: February 12, 2025

REFERENCES

1. Copray, J.C., Liem, R.S., Ter Horst, G.J., and van Willigen, J.D. (1990). Dopaminergic afferents to the mesencephalic trigeminal nucleus of the rat: a light and electron microscope immunocytochemistry study. Brain Res. *514*, 343–348. https://doi.org/10.1016/0006-8993(90)91430-o.
2. Krettek, J.E., and Price, J.L. (1978). Amygdaloid projections to subcortical structures within the basal forebrain and brainstem in the rat and cat. J. Comp. Neurol. *178*, 225–254. https://doi.org/10.1002/cne.901780204.
3. Nagy, J.I., Buss, M., and Daddona, P.E. (1986). On the innervation of trigeminal mesencephalic primary afferent neurons by adenosine

deaminase-containing projections from the hypothalamus in the rat. Neuroscience *17*, 141–156. https://doi.org/10.1016/0306-4522(86)90232-0.

4. Bae, Y.C., Park, K.P., Yoshida, A., Nakagawa, S., Kurata, S., Chen, K., Takemura, M., and Shigenaga, Y. (1997). Identification of gamma-aminobutyric acid-immunoreactive axon endings associated with mesencephalic periodontal afferent terminals and morphometry of the two types of terminals in the cat supratrigeminal nucleus. J. Comp. Neurol. *389*, 127–138. https://doi.org/10.1002/(sici)1096-9861(19971208)389:1<127::aid-cne9>3.0.co;2-4.
5. Buisseret-Delmas, C., Pinganaud, G., Compoint, C., and Buisseret, P. (1997). Projection from trigeminal nuclei to neurons of the mesencephalic trigeminal nucleus in rat. Neurosci. Lett. *229*, 189–192. https://doi.org/10.1016/s0304-3940(97)00452-7.
6. Rokx, J.T., Luiten, P.G., and Van Willigen, J.D. (1988). Afferent projections to the mesencephalic trigeminal nucleus in the rat. Anterograde tracing with Phaseolus vulgaris leukoagglutinin. Acta Anat. *132*, 260–264. https://doi.org/10.1159/000146584.
7. Ter Horst, G.J., Copray, J.C., Liem, R.S., and Van Willigen, J.D. (1991). Projections from the rostral parvocellular reticular formation to pontine and medullary nuclei in the rat: involvement in autonomic regulation and orofacial motor control. Neuroscience *40*, 735–758. https://doi.org/10.1016/0306-4522(91)90009-d.
8. Enomoto, A., Han, J.M., Hsiao, C.F., Wu, N., and Chandler, S.H. (2006). Participation of sodium currents in burst generation and control of membrane excitability in mesencephalic trigeminal neurons. J. Neurosci. *26*, 3412–3422. https://doi.org/10.1523/JNEUROSCI.5274-05.2006.
9. Enomoto, A., Seki, S., Tanaka, S., Ishihama, K., Yamanishi, T., Kogo, M., and Hamada, S. (2018). Development of resurgent and persistent sodium currents in mesencephalic trigeminal neurons. J. Neurosci. Res. *96*, 305–312. https://doi.org/10.1002/jnr.24134.
10. Pedroarena, C.M., Pose, I.E., Yamuy, J., Chase, M.H., and Morales, F.R. (1999). Oscillatory membrane potential activity in the soma of a primary afferent neuron. J. Neurophysiol. *82*, 1465–1476. https://doi.org/10.1152/jn.1999.82.3.1465.
11. Venugopal, S., Seki, S., Terman, D.H., Pantazis, A., Olcese, R., Wiedau-Pazos, M., and Chandler, S.H. (2019). Resurgent Na+ Current Offers Noise Modulation in Bursting Neurons. PLoS Comput. Biol. *15*, e1007154. https://doi.org/10.1371/journal.pcbi.1007154.
12. Wu, N., Enomoto, A., Tanaka, S., Hsiao, C.F., Nykamp, D.Q., Izhikevich, E., and Chandler, S.H. (2005). Persistent sodium currents in mesencephalic v neurons participate in burst generation and control of membrane excitability. J. Neurophysiol. *93*, 2710–2722. https://doi.org/10.1152/jn.00636.2004.
13. Akin, E.J., Solé, L., Dib-Hajj, S.D., Waxman, S.G., and Tamkun, M.M. (2015). Preferential targeting of Nav1.6 voltage-gated Na+ Channels to the axon initial segment during development. PLoS One *10*, e0124397. https://doi.org/10.1371/journal.pone.0124397.
14. Boiko, T., Rasband, M.N., Levinson, S.R., Caldwell, J.H., Mandel, G., Trimmer, J.S., and Matthews, G. (2001). Compact myelin dictates the differential targeting of two sodium channel isoforms in the same axon. Neuron *30*, 91–104. https://doi.org/10.1016/s0896-6273(01)00265-3.
15. Boiko, T., Van Wart, A., Caldwell, J.H., Levinson, S.R., Trimmer, J.S., and Matthews, G. (2003). Functional specialization of the axon initial segment by isoform-specific sodium channel targeting. J. Neurosci. *23*, 2306–2313. https://doi.org/10.1523/JNEUROSCI.23-06-02306.2003.
16. Gasser, A., Ho, T.S.Y., Cheng, X., Chang, K.J., Waxman, S.G., Rasband, M.N., and Dib-Hajj, S.D. (2012). An ankyrinG-binding motif is necessary and sufficient for targeting Nav1.6 sodium channels to axon initial segments and nodes of Ranvier. J. Neurosci. *32*, 7232–7243. https://doi.org/10.1523/JNEUROSCI.5434-11.2012.
17. Hu, W., Tian, C., Li, T., Yang, M., Hou, H., and Shu, Y. (2009). Distinct contributions of Na(v)1.6 and Na(v)1.2 in action potential initiation and backpropagation. Nat. Neurosci. *12*, 996–1002. https://doi.org/10.1038/nn.2359.
18. Osorio, N., Alcaraz, G., Padilla, F., Couraud, F., Delmas, P., and Crest, M. (2005). Differential targeting and functional specialization of sodium channels in cultured cerebellar granule cells. J. Physiol. *569*, 801–816. https://doi.org/10.1113/jphysiol.2005.097022.
19. Armstrong, C.M., and Cota, G. (1999). Calcium block of Na+ channels and its effect on closing rate. Proc. Natl. Acad. Sci. USA *96*, 4154–4157. https://doi.org/10.1073/pnas.96.7.4154.
20. Morquette, P., Verdier, D., Kadala, A., Féthière, J., Philippe, A.G., Robitaille, R., and Kolta, A. (2015). An astrocyte-dependent mechanism for neuronal rhythmogenesis. Nat. Neurosci. *18*, 844–854. https://doi.org/10.1038/nn.4013.
21. Ryczko, D., Hanini-Daoud, M., Condamine, S., Bréant, B.J.B., Fougère, M., Araya, R., and Kolta, A. (2021). S100beta-mediated astroglial control of firing and input processing in layer 5 pyramidal neurons of the mouse visual cortex. J. Physiol. *599*, 677–707. https://doi.org/10.1113/JP280501.
22. Lund, J.P., Sadeghi, S., Athanassiadis, T., Caram Salas, N., Auclair, F., Thivierge, B., Arsenault, I., Rompré, P., Westberg, K.G., and Kolta, A. (2010). Assessment of the potential role of muscle spindle mechanoreceptor afferents in chronic muscle pain in the rat masseter muscle. PLoS One *5*, e11131. https://doi.org/10.1371/journal.pone.0011131.
23. Yang, J., Xing, J.L., Wu, N.P., Liu, Y.H., Zhang, C.Z., Kuang, F., Han, V.Z., and Hu, S.J. (2009). Membrane current-based mechanisms for excitability transitions in neurons of the rat mesencephalic trigeminal nuclei. Neuroscience *163*, 799–810. https://doi.org/10.1016/j.neuroscience.2009.07.007.
24. Wu, N., Hsiao, C.F., and Chandler, S.H. (2001). Membrane resonance and subthreshold membrane oscillations in mesencephalic V neurons: participants in burst generation. J. Neurosci. *21*, 3729–3739. https://doi.org/10.1523/JNEUROSCI.21-11-03729.2001.
25. Enomoto, A., Han, J.M., Hsiao, C.F., and Chandler, S.H. (2007). Sodium currents in mesencephalic trigeminal neurons from Nav1.6 null mice. J. Neurophysiol. *98*, 710–719. https://doi.org/10.1152/jn.00292.2007.
26. Ogoma, Y., Kobayashi, H., Fujii, T., Kondo, Y., Hachimori, A., Shimizu, T., and Hatano, M. (1992). Binding study of metal ions to S100 protein: 43Ca, 25Mg, 67Zn and 39K n.m.r. Int. J. Biol. Macromol. *14*, 279–286. https://doi.org/10.1016/s0141-8130(05)80041-8.
27. Brocard, F., Shevtsova, N.A., Bouhadfane, M., Tazerart, S., Heinemann, U., Rybak, I.A., and Vinay, L. (2013). Activity-dependent changes in extracellular Ca2+ and K+ reveal pacemakers in the spinal locomotor-related network. Neuron *77*, 1047–1054. https://doi.org/10.1016/j.neuron.2013.01.026.
28. Rosker, C., Lohberger, B., Hofer, D., Steinecker, B., Quasthoff, S., and Schreibmayer, W. (2007). The TTX metabolite 4,9-anhydro-TTX is a highly specific blocker of the Na(v1.6) voltage-dependent sodium channel. Am. J. Physiol. Cell Physiol. *293*, C783–C789. https://doi.org/10.1152/ajpcell.00070.2007.
29. Kohrman, D.C., Harris, J.B., and Meisler, M.H. (1996). Mutation detection in the med and medJ alleles of the sodium channel Scn8a. Unusual splicing due to a minor class AT-AC intron. J. Biol. Chem. *271*, 17576–17581. https://doi.org/10.1074/jbc.271.29.17576.
30. Yang, Q., Hamberger, A., Khatibi, N., Stigbrand, T., and Haglid, K.G. (1996). Presence of S-100 beta in cholinergic neurones of the rat hindbrain. Neuroreport *7*, 3093–3099. https://doi.org/10.1097/00001756-199611250-00060.
31. Lee, P.R., Kim, J., Rossi, H.L., Chung, S., Han, S.Y., Kim, J., and Oh, S.B. (2023). Transcriptional profiling of dental sensory and proprioceptive trigeminal neurons using single-cell RNA sequencing. Int. J. Oral Sci. *15*, 45. https://doi.org/10.1038/s41368-023-00246-z.
32. Sakatani, S., Seto-Ohshima, A., Shinohara, Y., Yamamoto, Y., Yamamoto, H., Itohara, S., and Hirase, H. (2008). Neural-activity-dependent

release of S100B from astrocytes enhances kainate-induced gamma oscillations *in vivo*. J. Neurosci. *28*, 10928–10936. https://doi.org/10.1523/JNEUROSCI.3693-08.2008.

33. Luo, P.F., Wang, B.R., Peng, Z.Z., and Li, J.S. (1991). Morphological characteristics and terminating patterns of masseteric neurons of the mesencephalic trigeminal nucleus in the rat: an intracellular horseradish peroxidase labeling study. J. Comp. Neurol. *303*, 286–299. https://doi.org/10.1002/cne.903030210.
34. Xing, J.L., Hu, S.J., and Yang, J. (2014). Electrophysiological Features of Neurons in the Mesencephalic Trigeminal Nuclei. Neurosignals *22*, 79–91. https://doi.org/10.1159/000369822.
35. del Negro, C.A., Hsiao, C.F., and Chandler, S.H. (1999). Outward currents influencing bursting dynamics in guinea pig trigeminal motoneurons. J. Neurophysiol. *81*, 1478–1485. https://doi.org/10.1152/jn.1999.81.4.1478.
36. Dapino, A., Davoine, F., and Curti, S. (2023). D-type K+ current rules the function of electrically coupled neurons in a species-specific fashion. J. Gen. Physiol. *155*, e202313353. https://doi.org/10.1085/jgp.202313353.
37. Hermann, A., Donato, R., Weiger, T.M., and Chazin, W.J. (2012). S100 calcium binding proteins and ion channels. Front. Pharmacol. *3*, 67. https://doi.org/10.3389/fphar.2012.00067.
38. Saito, M., Murai, Y., Sato, H., Bae, Y.C., Akaike, T., Takada, M., and Kang, Y. (2006). Two opposing roles of 4-AP-sensitive K+ current in initiation and invasion of spikes in rat mesencephalic trigeminal neurons. J. Neurophysiol. *96*, 1887–1901. https://doi.org/10.1152/jn.00176.2006.
39. Wang, F., Smith, N.A., Xu, Q., Fujita, T., Baba, A., Matsuda, T., Takano, T., Bekar, L., and Nedergaard, M. (2012). Astrocytes modulate neural network activity by Ca(2)+-dependent uptake of extracellular K+. Sci. Signal. *5*, ra26. https://doi.org/10.1126/scisignal.2002334.
40. Van Wart, A., and Matthews, G. (2006). Impaired firing and cell-specific compensation in neurons lacking nav1.6 sodium channels. J. Neurosci. *26*, 7172–7180. https://doi.org/10.1523/JNEUROSCI.1101-06.2006.
41. Royeck, M., Horstmann, M.T., Remy, S., Reitze, M., Yaari, Y., and Beck, H. (2008). Role of axonal NaV1.6 sodium channels in action potential initiation of CA1 pyramidal neurons. J. Neurophysiol. *100*, 2361–2380. https://doi.org/10.1152/jn.90332.2008.
42. Chung, G., Saito, M., Kawasaki, Y., Kawano, T., Yin, D., Lee, S., Kogo, M., Takada, M., Bae, Y.C., Kim, J.S., et al. (2015). Generation of resonance-dependent oscillation by mGluR-I activation switches single spiking to bursting in mesencephalic trigeminal sensory neurons. Eur. J. Neurosci. *41*, 998–1012. https://doi.org/10.1111/ejn.12858.
43. Kang, Y., Saito, M., Sato, H., Toyoda, H., Maeda, Y., Hirai, T., and Bae, Y.C. (2007). Involvement of persistent Na+ current in spike initiation in primary sensory neurons of the rat mesencephalic trigeminal nucleus. J. Neurophysiol. *97*, 2385–2393. https://doi.org/10.1152/jn.01191.2006.
44. Rush, A.M., Dib-Hajj, S.D., and Waxman, S.G. (2005). Electrophysiological properties of two axonal sodium channels, Nav1.2 and Nav1.6, expressed in mouse spinal sensory neurones. J. Physiol. *564*, 803–815. https://doi.org/10.1113/jphysiol.2005.083089.
45. Smith, M.R., Smith, R.D., Plummer, N.W., Meisler, M.H., and Goldin, A.L. (1998). Functional analysis of the mouse Scn8a sodium channel. J. Neurosci. *18*, 6093–6102. https://doi.org/10.1523/JNEUROSCI.18-16-06093.1998.
46. Zybura, A., Hudmon, A., and Cummins, T.R. (2021). Distinctive Properties and Powerful Neuromodulation of Na(v)1.6 Sodium Channels Regulates Neuronal Excitability. Cells *10*, 1595. https://doi.org/10.3390/cells10071595.
47. Caldwell, J.H., Schaller, K.L., Lasher, R.S., Peles, E., and Levinson, S.R. (2000). Sodium channel Na(v)1.6 is localized at nodes of ranvier, dendrites, and synapses. Proc. Natl. Acad. Sci. USA *97*, 5616–5620. https://doi.org/10.1073/pnas.090034797.
48. Katz, E., Stoler, O., Scheller, A., Khrapunsky, Y., Goebbels, S., Kirchhoff, F., Gutnick, M.J., Wolf, F., and Fleidervish, I.A. (2018). Role of sodium channel subtype in action potential generation by neocortical pyramidal neurons. Proc. Natl. Acad. Sci. USA *115*, E7184–E7192. https://doi.org/10.1073/pnas.1720493115.
49. Palmer, L.M., and Stuart, G.J. (2006). Site of action potential initiation in layer 5 pyramidal neurons. J. Neurosci. *26*, 1854–1863. https://doi.org/10.1523/JNEUROSCI.4812-05.2006.
50. King, A.N., Manning, C.F., and Trimmer, J.S. (2014). A unique ion channel clustering domain on the axon initial segment of mammalian neurons. J. Comp. Neurol. *522*, 2594–2608. https://doi.org/10.1002/cne.23551.
51. Espino, C.M., Nagaraja, C., Ortiz, S., Dayton, J.R., Murali, A.R., Ma, Y., Mann, E.L., Garlapalli, S., Wohlgemuth, R.P., Brashear, S.E., et al. (2024). Differential encoding of mammalian proprioception by voltage-gated sodium channels. Preprint at bioRxiv. https://doi.org/10.1101/2024.08.27.609982.
52. Nascimento, A.I., Da Silva, T.F., Fernandes, E.C., Luz, L.L., Mar, F.M., Safronov, B.V., and Sousa, M.M. (2022). Sensory neurons have an axon initial segment that initiates spontaneous activity in neuropathic pain. Brain *145*, 1632–1640. https://doi.org/10.1093/brain/awac078.
53. Verdier, D., Lund, J.P., and Kolta, A. (2004). Synaptic inputs to trigeminal primary afferent neurons cause firing and modulate intrinsic oscillatory activity. J. Neurophysiol. *92*, 2444–2455. https://doi.org/10.1152/jn.00279.2004.
54. Hanani, M., and Spray, D.C. (2020). Emerging importance of satellite glia in nervous system function and dysfunction. Nat. Rev. Neurosci. *21*, 485–498. https://doi.org/10.1038/s41583-020-0333-z.
55. Zheng, Q., Dong, X., Green, D.P., and Dong, X. (2022). Peripheral mechanisms of chronic pain. Med. Rev. *2*, 251–270. https://doi.org/10.1515/mr-2022-0013.
56. Hanani, M. (2005). Satellite glial cells in sensory ganglia: from form to function. Brain Res. Brain Res. Rev. *48*, 457–476. https://doi.org/10.1016/j.brainresrev.2004.09.001.
57. Copray, J.C., Liem, R.S., and van Willigen, J.D. (1990). Morphological arrangement between astrocytes and trigeminal mesencephalic primary afferent neurons in the rat. Exp. Brain Res. *83*, 215–218. https://doi.org/10.1007/BF00232211.
58. Rusakov, D.A., and Fine, A. (2003). Extracellular Ca2+ depletion contributes to fast activity-dependent modulation of synaptic transmission in the brain. Neuron *37*, 287–297. https://doi.org/10.1016/s0896-6273(03)00025-4.
59. Smith, S.J. (1992). Do astrocytes process neural information? Prog. Brain Res. *94*, 119–136. https://doi.org/10.1016/s0079-6123(08)61744-6.
60. Amir, R., Kocsis, J.D., and Devor, M. (2005). Multiple interacting sites of ectopic spike electrogenesis in primary sensory neurons. J. Neurosci. *25*, 2576–2585. https://doi.org/10.1523/JNEUROSCI.4118-04.2005.
61. Campero, M., Serra, J., Marchettini, P., and Ochoa, J.L. (1998). Ectopic impulse generation and autoexcitation in single myelinated afferent fibers in patients with peripheral neuropathy and positive sensory symptoms. Muscle Nerve *21*, 1661–1667. https://doi.org/10.1002/(sici)1097-4598(199812)21:12<1661::aid-mus6>3.0.co;2-n.
62. Han, H.C., Lee, D.H., and Chung, J.M. (2000). Characteristics of ectopic discharges in a rat neuropathic pain model. Pain *84*, 253–261. https://doi.org/10.1016/s0304-3959(99)00219-5.
63. Xiao, W.H., and Bennett, G.J. (2008). C-fiber spontaneous discharge evoked by chronic inflammation is suppressed by a long-term infusion of lidocaine yielding nanogram per milliliter plasma levels. Pain *137*, 218–228. https://doi.org/10.1016/j.pain.2008.02.018.
64. Berlinguer-Palmini, R., Narducci, R., Merhan, K., Dilaghi, A., Moroni, F., Masi, A., Scartabelli, T., Landucci, E., Sili, M., Schettini, A., et al. (2014). Arrays of microLEDs and astrocytes: biological amplifiers to optogenetically modulate neuronal networks reducing light requirement. PLoS One *9*, e108689. https://doi.org/10.1371/journal.pone.0108689.
65. Chen, J., Tan, Z., Zeng, L., Zhang, X., He, Y., Gao, W., Wu, X., Li, Y., Bu, B., Wang, W., and Duan, S. (2013). Heterosynaptic long-term depression

mediated by ATP released from astrocytes. Glia *61*, 178–191. https://doi.org/10.1002/glia.22425.

66. Gourine, A.V., Kasymov, V., Marina, N., Tang, F., Figueiredo, M.F., Lane, S., Teschemacher, A.G., Spyer, K.M., Deisseroth, K., and Kasparov, S. (2010). Astrocytes control breathing through pH-dependent release of ATP. Science *329*, 571–575. https://doi.org/10.1126/science.1190721.
67. Li, D., Hérault, K., Isacoff, E.Y., Oheim, M., and Ropert, N. (2012). Optogenetic activation of LiGluR-expressing astrocytes evokes anion channel-mediated glutamate release. J. Physiol. *590*, 855–873. https://doi.org/10.1113/jphysiol.2011.219345.
68. Perea, G., Yang, A., Boyden, E.S., and Sur, M. (2014). Optogenetic astrocyte activation modulates response selectivity of visual cortex neurons *in vivo*. Nat. Commun. *5*, 3262. https://doi.org/10.1038/ncomms4262.
69. Poskanzer, K.E., and Yuste, R. (2016). Astrocytes regulate cortical state switching *in vivo*. Proc. Natl. Acad. Sci. USA *113*, E2675–E2684. https://doi.org/10.1073/pnas.1520759113.
70. Shen, W., Nikolic, L., Meunier, C., Pfrieger, F., and Audinat, E. (2017). An autocrine purinergic signaling controls astrocyte-induced neuronal excitation. Sci. Rep. *7*, 11280. https://doi.org/10.1038/s41598-017-11793-x.
71. Tan, Z., Liu, Y., Xi, W., Lou, H.F., Zhu, L., Guo, Z., Mei, L., and Duan, S. (2017). Glia-derived ATP inversely regulates excitability of pyramidal and CCK-positive neurons. Nat. Commun. *8*, 13772. https://doi.org/10.1038/ncomms13772.
72. Muller, P., Draguhn, A., and Egorov, A.V. (2018). Persistent sodium current modulates axonal excitability in CA1 pyramidal neurons. J. Neurochem. *146*, 446–458. https://doi.org/10.1111/jnc.14479.
73. Baker, R., and Llinás, R. (1971). Electrotonic coupling between neurones in the rat mesencephalic nucleus. J. Physiol. *212*, 45–63. https://doi.org/10.1113/jphysiol.1971.sp009309.
74. Curti, S., Hoge, G., Nagy, J.I., and Pereda, A.E. (2012). Synergy between electrical coupling and membrane properties promotes strong synchronization of neurons of the mesencephalic trigeminal nucleus. J. Neurosci. *32*, 4341–4359. https://doi.org/10.1523/JNEUROSCI.6216-11.2012.
75. Nagy, J.I., and Lynn, B.D. (2018). Structural and Intermolecular Associations Between Connexin36 and Protein Components of the Adherens Junction-Neuronal Gap Junction Complex. Neuroscience *384*, 241–261. https://doi.org/10.1016/j.neuroscience.2018.05.026.
76. Curti, S., Davoine, F., and Dapino, A. (2022). Function and Plasticity of Electrical Synapses in the Mammalian Brain: Role of Non-Junctional Mechanisms. Biology *11*, 81. https://doi.org/10.3390/biology11010081.
77. Davoine, F., and Curti, S. (2019). Response to coincident inputs in electrically coupled primary afferents is heterogeneous and is enhanced by H-current (IH) modulation. J. Neurophysiol. *122*, 151–175. https://doi.org/10.1152/jn.00029.2019.
78. Debanne, D., and Rama, S. (2011). Astrocytes shape axonal signaling. Sci. Signal. *4*, pe11. https://doi.org/10.1126/scisignal.2001884.
79. Condamine, S., Lavoie, R., Verdier, D., and Kolta, A. (2018). Functional rhythmogenic domains defined by astrocytic networks in the trigeminal main sensory nucleus. Glia *66*, 311–326. https://doi.org/10.1002/glia.23244.
80. Westberg, K.G., Kolta, A., Clavelou, P., Sandström, G., and Lund, J.P. (2000). Evidence for functional compartmentalization of trigeminal muscle spindle afferents during fictive mastication in the rabbit. Eur. J. Neurosci. *12*, 1145–1154. https://doi.org/10.1046/j.1460-9568.2000.00001.x.
81. Kolta, A., Lund, J.P., Westberg, K.G., and Clavelou, P. (1995). Do muscle-spindle afferents act as interneurons during mastication? Trends Neurosci. *18*, 441. https://doi.org/10.1016/0166-2236(95)94493-o.
82. Verdier, D., Lund, J.P., and Kolta, A. (2003). GABAergic control of action potential propagation along axonal branches of mammalian sensory neurons. J. Neurosci. *23*, 2002–2007. https://doi.org/10.1523/JNEUROSCI.23-06-02002.2003.
83. Christensen, R.K., Delgado-Lezama, R., Russo, R.E., Lind, B.L., Alcocer, E.L., Rath, M.F., Fabbiani, G., Schmitt, N., Lauritzen, M., Petersen, A.V., et al. (2018). Spinal dorsal horn astrocytes release GABA in response to synaptic activation. J. Physiol. *596*, 4983–4994. https://doi.org/10.1113/JP276562.
84. Sas, D., Gaudel, F., Verdier, D., and Kolta, A. (2024). Hyperexcitability of muscle spindle afferents in jaw-closing muscles in experimental myalgia: Evidence for large primary afferents involvement in chronic pain. Exp. Physiol. *109*, 100–111. https://doi.org/10.1113/EP090769.
85. Agulhon, C., Sun, M.Y., Murphy, T., Myers, T., Lauderdale, K., and Fiacco, T.A. (2012). Calcium Signaling and Gliotransmission in Normal vs. Reactive Astrocytes. Front. Pharmacol. *3*, 139. https://doi.org/10.3389/fphar.2012.00139.
86. Tanga, F.Y., Raghavendra, V., Nutile-McMenemy, N., Marks, A., and Deleo, J.A. (2006). Role of astrocytic S100beta in behavioral hypersensitivity in rodent models of neuropathic pain. Neuroscience *140*, 1003–1010. https://doi.org/10.1016/j.neuroscience.2006.02.070.
87. Stefani, L.C., Leite, F.M., da Graça L Tarragó, M., Zanette, S.A., de Souza, A., Castro, S.M., and Caumo, W. (2019). BDNF and serum S100B levels according the spectrum of structural pathology in chronic pain patients. Neurosci. Lett. *706*, 105–109. https://doi.org/10.1016/j.neulet.2019.05.021.
88. Teepker, M., Munk, K., Mylius, V., Haag, A., Möller, J.C., Oertel, W.H., and Schepelmann, K. (2009). Serum concentrations of s100b and NSE in migraine. Headache *49*, 245–252. https://doi.org/10.1111/j.1526-4610.2008.01228.x.
89. Zanette, S.A., Dussan-Sarria, J.A., Souza, A., Deitos, A., Torres, I.L.S., and Caumo, W. (2014). Higher serum S100B and BDNF levels are correlated with a lower pressure-pain threshold in fibromyalgia. Mol. Pain *10*, 46. https://doi.org/10.1186/1744-8069-10-46.
90. Lezmy, J., Arancibia-Cárcamo, I.L., Quintela-López, T., Sherman, D.L., Brophy, P.J., and Attwell, D. (2021). Astrocyte Ca(2+)-evoked ATP release regulates myelinated axon excitability and conduction speed. Science *374*, eabh2858. https://doi.org/10.1126/science.abh2858.
91. Sasaki, T., Matsuki, N., and Ikegaya, Y. (2011). Action-potential modulation during axonal conduction. Science *331*, 599–601. https://doi.org/10.1126/science.1197598.
92. Dutta, D.J., Woo, D.H., Lee, P.R., Pajevic, S., Bukalo, O., Huffman, W.C., Wake, H., Basser, P.J., SheikhBahaei, S., Lazarevic, V., et al. (2018). Regulation of myelin structure and conduction velocity by perinodal astrocytes. Proc. Natl. Acad. Sci. USA *115*, 11832–11837. https://doi.org/10.1073/pnas.1811013115.
93. Falardeau, D., Dubois, S., and Kolta, A. (2023). The coordination of chewing. Curr. Opin. Neurobiol. *83*, 102805. https://doi.org/10.1016/j.conb.2023.102805.
94. Mameli, O., Caria, M.A., Biagi, F., Zedda, M., and Farina, V. (2017). Neurons within the trigeminal mesencephalic nucleus encode for the kinematic parameters of the whisker pad macrovibrissae. Physiol. Rep. *5*, e13206. https://doi.org/10.14814/phy2.13206.
95. Mameli, O., Stanzani, S., Mulliri, G., Pellitteri, R., Caria, M.A., Russo, A., and De Riu, P. (2010). Role of the trigeminal mesencephalic nucleus in rat whisker pad proprioception. Behav. Brain Funct. *6*, 69. https://doi.org/10.1186/1744-9081-6-69.
96. Fortin, S.M., Chen, J., Grill, H.J., and Hayes, M.R. (2021). The Mesencephalic Trigeminal Nucleus Controls Food Intake and Body Weight via Hindbrain POMC Projections. Nutrients *13*, 1642. https://doi.org/10.3390/nu13051642.
97. Zhao, Y.J., Liu, Y., Wang, J., Li, Q., Zhang, Z.M., Tu, T., Lei, R., Zhang, M., and Chen, Y.J. (2022). Activation of the Mesencephalic Trigeminal Nucleus Contributes to Masseter Hyperactivity Induced by Chronic Restraint Stress. Front. Cell. Neurosci. *16*, 841133. https://doi.org/10.3389/fncel.2022.841133.
98. Andrisani, G., and Andrisani, G. (2023). Sleep apnea pathophysiology. Sleep Breath. *27*, 2111–2122. https://doi.org/10.1007/s11325-023-02783-7.

99. Octeau, J.C., Gangwani, M.R., Allam, S.L., Tran, D., Huang, S., Hoang-Trong, T.M., Golshani, P., Rumbell, T.H., Kozloski, J.R., and Khakh, B.S. (2019). Transient, Consequential Increases in Extracellular Potassium Ions Accompany Channelrhodopsin2 Excitation. Cell Rep. *27*, 2249–2261.e7. https://doi.org/10.1016/j.celrep.2019.04.078.

100. Rungta, R.L., Osmanski, B.F., Boido, D., Tanter, M., and Charpak, S. (2017). Light controls cerebral blood flow in naive animals. Nat. Commun. *8*, 14191. https://doi.org/10.1038/ncomms14191.

101. Ichikawa, H., Jacobowitz, D.M., and Sugimoto, T. (1997). S100 protein-immunoreactive primary sensory neurons in the trigeminal and dorsal root ganglia of the rat. Brain Res. *748*, 253–257. https://doi.org/10.1016/s0006-8993(96)01364-9.

102. Maeda, T., Ochi, K., Nakakura-Ohshima, K., Youn, S.H., and Wakisaka, S. (1999). The Ruffini ending as the primary mechanoreceptor in the periodontal ligament: its morphology, cytochemical features, regeneration, and development. Crit. Rev. Oral Biol. Med. *10*, 307–327. https://doi.org/10.1177/10454411990100030401.

103. Nakakura-Ohshima, K., Hayashi, S., Atsumi, Y., Wakisaka, S., Nozawa-Inoue, K., and Maeda, T. (1998). Immunocytochemical detection of S-100beta in the periodontal Ruffini endings in the rat incisor. Neurosci. Lett. *258*, 163–166. https://doi.org/10.1016/s0304-3940(98)00872-6.

104. Khaliq, Z.M., Gouwens, N.W., and Raman, I.M. (2003). The contribution of resurgent sodium current to high-frequency firing in Purkinje neurons: an experimental and modeling study. J. Neurosci. *23*, 4899–4912. https://doi.org/10.1523/JNEUROSCI.23-12-04899.2003.

105. Garcia, A.D.R., Doan, N.B., Imura, T., Bush, T.G., and Sofroniew, M.V. (2004). GFAP-expressing progenitors are the principal source of constitutive neurogenesis in adult mouse forebrain. Nat. Neurosci. *7*, 1233–1241. https://doi.org/10.1038/nn1340.

106. Madisen, L., Mao, T., Koch, H., Zhuo, J.m., Berenyi, A., Fujisawa, S., Hsu, Y.W.A., Garcia, A.J., 3rd, Gu, X., Zanella, S., et al. (2012). A toolbox of Cre-dependent optogenetic transgenic mice for light-induced activation and silencing. Nat. Neurosci. *15*, 793–802. https://doi.org/10.1038/nn.3078.

107. Kafitz, K.W., Meier, S.D., Stephan, J., and Rose, C.R. (2008). Developmental profile and properties of sulforhodamine 101–Labeled glial cells in acute brain slices of rat hippocampus. J. Neurosci. Methods *169*, 84–92. https://doi.org/10.1016/j.jneumeth.2007.11.022.

STAR★METHODS

KEY RESOURCES TABLE

REAGENT or RESOURCE	SOURCE	IDENTIFIER
Antibodies		
Mouse anti-S100β	Sigma-Aldrich	Cat# S2532; RRID: AB_477499
Rabbit anti-Nav1.6	Alomone Labs	Cat# ASC-009; RRID: AB_2040202
Sheep anti-Parvalbumin	Thermo Fisher Scientific	Cat# PA5-47693; RRID: AB_2609239
Donkey anti-sheep DyLight 405	Jackson ImmunoResearch Labs	Cat# 713-475-003; RRID: AB_2340739
Donkey anti-rabbit Alexa Fluor 488	Jackson ImmunoResearch Labs	Cat# 711-545-152; RRID: AB_2313584
Donkey anti-mouse Alexa Fluor 488	Jackson ImmunoResearch Labs	Cat# 715-545-151; RRID: AB_2341099
Donkey anti-rabbit Alexa Fluor 555	Thermo Fisher Scientific	Cat# A-31572; RRID: AB_162543
Donkey anti-mouse Alexa Fluor 594	Jackson ImmunoResearch Labs	Cat# 715-585-150; RRID: AB_2340854
Chemicals, peptides, and recombinant proteins		
Potassium chloride	Fisher Scientific	#P217-500
Potassium phosphate monobasic	Fisher Scientific	#P285-500
Magnesium sulfate anhydrous	Fisher Scientific	#M65-500
Sodium bicarbonate	Fisher Scientific	#S233-500
Dextrose	Fisher Scientific	#D16-500
Calcium chloride dihydrate	Fisher Scientific	#C70-500
Sucrose	Sigma-Aldrich	#S9378
Sodium chloride	Fisher Scientific	#S671-3
Potassium D-gluconate	Sigma-Aldrich	#G4500-100G
Magnesium chloride	Sigma-Aldrich	#68475-100ML-F
HEPES	Sigma-Aldrich	#H3375-100G
EGTA	Sigma-Aldrich	#E4378
Tris ATP salt	Sigma-Aldrich	#A9062
Tris GTP salt	Sigma-Aldrich	#G9002
Alexa Fluor 488 hydrazide	Invitrogen	#A10436
Alexa Fluor 594 hydrazide	Invitrogen	#A10438
Riluzole	Tocris Bioscience	#0768
4,9-anhydro-tetrodotoxin	Cayman Chemical co.	#19084
CNQX	Tocris Bioscience	# 1045/10
D,L-2amino-5 phosphonovaleric acid	Tocris Bioscience	#0106/10
SR 95531 hydrobromide	Tocris Bioscience	#1262
S100β	Inixium Inc.	
1,2-Bis(2-aminophenoxy)-ethane-N,N,N',N'-tetraacetic acid, tetrasodium salt hydrate	ThermoFisher Scientific	#401650010
Paraformaldehyde	Fisher Scientific	#AC416785000
Sucrose	Sigma-Aldrich	#S9378
Triton-X100	Sigma-Aldrich	#T8787
Normal donkey serum	Jackson ImmunoResearch	#017-000-121
Fluoromount-G	Invitrogen	#00-4958-02
Experimental models: Organisms/strains		
C57BL/6J mice	Bred in house after obtaining from The Jackson Laboratory	RRID: IMSR_JAX:000664
C3Fe.Cg-Scn8a$^{med/J}$ mice	Bred in house after obtaining from The Jackson Laboratory	RRID: IMSR_JAX:003798

(*Continued on next page*)

Continued

REAGENT or RESOURCE	SOURCE	IDENTIFIER
B6.Cg-Tg(Gfap-cre)73.12Mvs/J mice	Bred in house after obtaining from The Jackson Laboratory	RRID: IMSR_JAX:012886
B6.Cg-Gt(ROSA)26Sortm32(CAG COP4*H134R/EYFP)Hze/J mice	Bred in house after obtaining from The Jackson Laboratory	RRID: IMSR_JAX:024109
GFAP-ChR2-EYFP mice	Bred in house	N/A
Oligonucleotides		
19574: TCA GGA GCA AGG TTC TAG GC	Alpha ADN, S.E.N.C.	#649995
19575: AGG AGT GGC GCT AAA TCT GA	Alpha ADN, S.E.N.C.	#649996
19576: TAC CAA AAG TCC CCA TAC CC	Alpha ADN, S.E.N.C.	#649997
Cre_seqF1: TCGACCAGGTTCGTTCACTC	Alpha ADN, S.E.N.C.	#678698
Cre_seqR2: CTGACCCGGCAAAACAGGTA	Alpha ADN, S.E.N.C.	#678699
Chim_F: AGGGCTTTCCTTGCTGTGTC	Alpha ADN, S.E.N.C.	#678700
Chim_R : TAGGTCCCTTCTCATGAACC	Alpha ADN, S.E.N.C.	#678701
Software and algorithms		
Fluoview 2	Olympus	#F10SWARS2
pClamp 8	Molecular Devices	#6190-013
Clampfit 10	Molecular Devices	https://www.moleculardevices.com/products
MultiClamp	Molecular Devices	https://www.moleculardevices.com/products
SPSS 26-29	IBM	IBM SPSS Statistic
ImageJ	National Institute of Health	https://imagej.net/ij/index.html

EXPERIMENTAL MODEL AND STUDY PARTICIPANT DETAILS

All experiments were conducted according to the Canadian Institutes of Health Research rules and were approved by the Animal Care and Use Committee of Université de Montréal.

A total of 137 mice were used, including 5 GFAP-cre mice (B6.Cg-Tg(Gfap-cre)73.12Mvs/J, stock 12886, JAX), 51 wild-type mice (C57BL/6J, Stock 000664, JAX), 7 Nav1.6 null mice, 71 mice expressing the channelrhodopsin 2 (ChR2) under the control of the GFAP promoter (GFAP-ChR2-EYFP mice) and 3 mice expressing the channelrhodopsin 2 (ChR2) under the control of the Parvalbumin promoter (Pvalb-TdTomato-ChR2-EYFP mice). Nav1.6 null mice were obtained by crossing heterozygous Scn8amed mice (C3Fe.Cg-Scn8amed/J, stock 003798, JAX;[29,104]) and selecting the homozygous offsprings. GFAP-ChR2-EYFP mice were produced by crossing GFAP-Cre (B6.Cg-Tg(Gfap-cre)73.12Mvs/J, stock 12886, JAX;[105]) and ChR2-lox mice (B6.Cg-Gt(ROSA)26Sortm32(CAG COP4*H134R/EYFP)Hze/J, stock 24109, JAX;[106]). Pvalb-TdTomato-ChR2-EYFP mice were produced by crossing Pvalb-cre-tdTomato mice (graciously supplied by Reza Sharif-Naeini, but originally generated by crossing commercially available PVcre mice (JAX, stock #017320) with Ai14 tdTomato reporter (JAX, stock#007914) and ChR2-lox mice (B6.Cg-Gt(ROSA)26Sortm32(CAG COP4*H134R/EYFP)Hze/J, stock 24109, JAX).

METHOD DETAILS

Brainstem slice preparation

Coronal brainstem slices (325-350 μm) were prepared from mice aged from 14 to 21 days. The mice were anesthetized by inhalation of isoflurane (Pharmaceutical Partners of Canada Inc., Richmond Hill, ON, Canada) prior to decapitation. Their brain was quickly extracted from the cranium and sectioned in an ice-cold modified artificial cerebrospinal fluid (CSF, in mM: 3 KCl, 1.25 $KH2PO_4$, 4 $MgSO_4$, 26 $NaHCO_3$, 10 Dextrose, 0.2 $CaCl_2$, 219 Sucrose, pH 7.3-7.4, 300-320 mOsmol/kg) saturated with a mix of 95% O_2 and 5% CO_2 using a VT1000S vibratome (Leica). Slices were transferred to a submerged chamber and continuously perfused with artificial CSF (in mM: 124 NaCl, 3 KCl, 1.25 KH_2PO_4, 1.3 $MgSO_4$, 26 $NaHCO_3$, 10 Dextrose, and 1.6 $CaCl_2$, pH 7.3-7.4, 294-300 mOsmol/kg) bubbled with 95% O_2 and 5% CO_2 at room temperature. Slices were allowed to rest for a minimum of one hour before recording. In some experiments, after sectioning, the brainstem slices were incubated for 20 min at 34°C in a chamber filled with aCSF containing 1 μM Sulforhodamine-101 to label astrocytes following the procedure of Kafitz et al.[107] The slices were then transferred to a second chamber to rinse out excess SR-101 from the tissue. They were kept at room temperature until needed.

Electrophysiology and analysis

Recordings were carried out at room temperature in a submerged chamber continually perfused with artificial CSF bubbled with 95% O_2 and 5% CO_2. Patch microelectrodes were pulled from borosilicate glass capillaries (1.5 mm outside diameter, 1.12 mm inside diameter, World Precision Instruments) using a P-97 puller (Sutter Instruments). For neuronal recordings, pipettes (resistance 6-10 MΩ) were filled with an internal solution containing (in mM): 140 K-gluconate, 5 NaCl, 2 $MgCl_2$, 10 HEPES, 0.5 EGTA, 2 Tris ATP salt, 0.4 Tris GTP salt, pH 7.2-7.3, 280-300mOsmol/kg. 0.05 Alexa Fluor 488 or 594 was added to the internal solution to visualize neuronal and axonal morphologies during the experiment. Confocal imaging was performed using an Olympus Fluoview FV 1000 confocal microscope equipped with a 40x (N.A. 0.80) water immersion objective. All recordings were performed using a Multiclamp 700A amplifier, Digidata 1322A interface coupled to a computer equipped with pClamp 8 software (Molecular Devices, San Jose, CA). After the establishment of a gigaseal, the membrane potential was held at -60 mV, and the membrane patch was suctioned. The pipette resistance and capacitance were compensated electronically. Neurons were discarded when action potentials did not overshoot 0 mV or when the resting membrane potential was depolarized (>-45 mV). Recordings were analyzed using standard scripts in Clampfit. The neuronal passive properties included the resting membrane potential (in mV), the input resistance (in MΩ), and the firing threshold. The resting membrane potential was measured when no current was injected into the recorded neuron in current-clamp mode. The input resistance was determined as the voltage change induced by a small hyperpolarizing current (−20 to−40 pA) of 1 s duration applied from resting membrane potential divided by the amount of injected current. Firing patterns and membrane rectification were described from the current-voltage (I-V) curve obtained in the current-clamp mode.

Optogenetic stimulation

Astrocytes or neurons were optogenetically stimulated with two lasers (440 and 488 nm) used simultaneously in the SIM lightpath of an FV1000 microscope (Olympus) in mice expressing the channelrhodopsin (ChR2) under the control of the GFAP promoter (GFAP-Cre/ChR2-lox). The SIM scanner was used in the 'tornado' scanning mode (a spiraling scan mode) to photoactivate manually delineated small areas surrounding the recorded neuron. Optogenetic stimulations were applied using 5-30 s pulses (10-20% laser power/8.6-14.9 μW for laser 440 nm/8.7-15.9 μW for laser 488 nm). To assess the specificity of wavelength in activating astrocytes, 559 nm laser pulses (10-20% laser power/120-200 μW) were applied in control experiments.

Drug application

Chemicals used in this study were purchased from Sigma-Aldrich (Oakville, Ontario, Canada), Tocris Biosciences (Ellisville, Missouri, USA), Abcam (Cambridge, UK), and Inixium (Laval, Quebec, Canada). The following drugs were bath-applied using a syringe pump: 4,9-anhydro-tetrodotoxin (4,9-anhydro-TTX, 100 nM), CNQX (10 μM), D,L-2amino-5 phosphonovaleric acid (APV, 75 μM), SR 95531 hydrobromide (Gabazine, 20 μM). In some experiments, aCSF or the Ca^{2+}-binding proteins S100β (129 μM) or 1,2-bis(o-aminophenoxy)ethane-N,N,N′,N′-tetraacetic acid tetrasodium salt (BAPTA, 5 mM) were locally applied with glass micropipettes (tip diameter around 1 μm) with 2-20 psi pressure pulses of variable duration (1-30 s; Picospritzer III, Parker Instrumentation, Fairfield NJ USA). Monoclonal anti-S100β antibodies (mouse anti-S100β, Sigma Aldrich #S2532 or rabbit anti-S100β, Abcam ab56642) were applied locally with large-tip (10-20 μm) glass micropipettes carefully lowered near the recorded neuron with 0.1-2 psi pressure pulses lasting from 5 to 20 minutes. All bath-applied chemicals were diluted in water at 100X their final concentrations and further diluted through the perfusing aCSF at their final concentrations. Except for S100β, all locally applied chemicals were diluted at their final concentrations in aCSF. S100β was diluted in a 20 mM HEPES buffer containing 140 mM of NaCl but no Ca^{2+}, at pH 7.4.

Immunohistochemistry

For the immunohistochemistry against S100β and Nav1.6, coronal brainstem slices (500 μm) were prepared from 14 to 21-day-old wild-type (N=6) or $Na_v1.6$-null mice (N=2) using a vibratome VT 1000S (Leica), immediately immersed in a solution of 4% (wt/vol) paraformaldehyde in PBS and kept overnight at 4°C. For cryoprotection, the slices were then immersed in a solution of 20% sucrose in PBS for two hours at 4°C. Using a sliding microtome (Leica SM20000R), 40 μm thick sections of the brainstem were made. The sections were rinsed 3 times for 10 minutes in PBS and incubated in a blocking solution containing 0.3% Triton X-100 and 10% Normal Donkey Serum (Jackson ImmunoResearch #017-000-121) in PBS for two hours at room temperature. The sections were then rinsed 3 times for 10 minutes in PBS and incubated overnight at 4°C in a mix of the primary antibodies (mouse anti-S100β, Sigma Aldrich #S2532, dilution 1:400; rabbit anti-Nav1.6, Alomone lab #ASC-009, dilution 1:400). The following day, the slices were rinsed 3 times for 5 minutes in PBS and incubated in the relevant secondary antibodies mix (donkey anti-rabbit-Alexa Fluor 488, Jackson Immunoresearch #711-545-152, dilution 1:500; donkey anti-mouse Alexa Fluor 488, Jackson Immunoresearch #715-545-151, dilution 1:500; donkey anti-rabbit Alexa Fluor 555, Invitrogen #A31572, dilution 1:500; donkey anti-mouse-Alexa Fluor 594, Jackson Immunoresearch #715-585-150, dilution 1:500) diluted in the blocking solution for 60 minutes in a dark chamber at room temperature. For the immunohistochemistry against Parvalbumin and S100β or the immunohistochemistry against Parvalbumin, S100β and GFP, coronal brainstem slices (350 μm) were prepared from 14 to 21-day-old wild-type (N=1), GFAP-cre (N=2) and GFAP-ChR2-EYFP (N=3) mice using a vibratome VT 1000S (Leica), immediately immersed in a solution of 4% (wt/vol) paraformaldehyde in PBS and kept overnight at 4°C. The slices were not re-sectioned. The primary antibodies used were mouse anti-S100β (Sigma Aldrich #S2532, dilution 1:400), chicken anti-GFP (Abcam #ab13970, dilution 1:1000), sheep anti-Parvalbumin (ThermoFisher, PA47693, dilution 1:40) and guinea-pig anti-Parvalbumin (Synaptic Systems, #195-004, dilution 1:400). The secondary antibodies used were donkey anti-mouse

Alexa Fluor 647 (Abcam #ab150107, dilution 1:500), donkey anti-chicken Alexa Fluor 488 (Jackson Immunoresearch #703-545-155, dilution 1:500), donkey anti-sheep Alexa Fluor 405 (Jackson Immunoresearch #713-475-003, dilution 1:500) and donkey anti-guinea pig Alexa Fluor 594 (Jackson Immunoresearch, #706-585-148, dilution 1:500). The incubation period with the secondary antibodies was 120 minutes. The sections were then rinsed 3 times for 5 minutes in PBS and mounted on ColorFrost Plus slides (Fisher Scientific, Ottawa, Ontario, Canada) using Fluoromount-G (Southern Biotech, Birmingham, Alabama, USA). Slides imaging was done using either an E600 epifluorescence microscope equipped with aDXM1200 digital camera (Nikon), an FV1000 confocal microscope (Olympus), or a TCS SP8 STED nanoscope (Leica). In all cases, a negative control was performed by removing the primary antibody and the absence of specific labeling on brainstem sections was confirmed. Images were treated with ImageJ (NIH) software to combine pictures and adjust the levels so that all fluorophores were clearly visible simultaneously.

QUANTIFICATION AND STATISTICAL ANALYSIS

Data are presented as mean ± standard error to the mean (SEM) and as proportions (%). Our sample sizes are comparable to those employed in the field and were not predetermined by any statistical methods. Our experimental paradigms necessitated no blinding or randomization procedures. For pairwise comparisons of normally distributed data, paired *t*-tests or independent *t*-tests were used. For pairwise comparisons of non-normally distributed data, the Wilcoxon Signed-Rank, or the Kruskall Wallis tests were used. Statistical significance was defined as $P < 0.05$. Data analysis was performed using SPSS.